

GAS DIFFUSION IN STRONGLY CONFINING AND INTERACTING MICROPOROUS
SORBENTS BY NMR

By

AKSHITA RANJAN DUTTA

A DISSERTATION PRESENTED TO THE GRADUATE SCHOOL
OF THE UNIVERSITY OF FLORIDA IN PARTIAL FULFILLMENT
OF THE REQUIREMENTS FOR THE DEGREE OF
DOCTOR OF PHILOSOPHY

UNIVERSITY OF FLORIDA

2017

© 2017 Akshita Ranjan Dutta

To my Mom, Dad, and younger brother for their sacrifices and encouragement
throughout my education

ACKNOWLEDGMENTS

I would like to acknowledge the guidance and mentorship of my doctoral co-advisors, Dr. Sergey Vasenkov and Dr. Kirk J. Ziegler for advancing my skills as an engineer, a researcher, and a contributor to the scientific community. The constant and unwavering support, and the time they have devoted to my graduate studies has been invaluable throughout this journey. I would like to thank Poorvajan Sekar for his assistance in the completion of this research during his graduate studies. I would also like to thank my lab mates, Dr. Robert Mueller, Evan Forman, and Matthias Trujillo for their support.

Being a part of the Energy Frontiers Research Center has been a priceless experience. I would like to thank all the graduate students and post-doctoral researchers of this center for their companionship and insights. The cooperation of the following collaborators, who are also members of the center is especially appreciated: Dr. David Sholl for his advice and guidance with respect to the single-file diffusion and hydrogen sulfide work; Dr. Ryan Lively, Dr. J R Schmidt and Guanghui Zhu for all work in relation to hydrogen sulfide.

I would like to thank Dr. James Collins at the Advanced Magnetic Resonance Imaging and Spectroscopy (AMRIS) facility for his technical assistance and expert input offered during the development of the new methodology.

I am indebted to my mother, Mini Dutta, and father, Ranjan Dutta, for their emotional support and their unaltered confidence in me. I would also like to thank my brother for his constant encouragement. The support of my family and friends throughout my doctoral studies is unparalleled and I would like to acknowledge their contribution in helping me achieve my goals: Pushpa Mohan, Yash Pal Dutta, Kanta

Dutta, Himani Nadgauda, Lauren Miller, Nicole Taylor, Subit Chakrabarti, Shreyas Honrao, Abhinav Bhandari, Yash Mehta, Arati Sakhalkar, Sharvari Bhagwat.

I am grateful to acknowledge the financial support of the Donors of the American Chemical Society Petroleum Research Fund (PRF#53140-ND10), NSF grant NO. CHE-0957641 and the NSF CAREER award No. CBET-0957641 for this work. A portion of this work was performed in the McKnight Brain Institute at the National High Magnetic Field Laboratory's AMRIS Facility, which is supported by National Science Foundation Cooperative Agreement No. DMR-1157490 and the State of Florida.

TABLE OF CONTENTS

	<u>page</u>
ACKNOWLEDGMENTS.....	4
LIST OF TABLES.....	8
LIST OF FIGURES.....	9
LIST OF SYMBOLS	11
LIST OF ABBREVIATIONS.....	13
ABSTRACT	14
CHAPTER	
1 INTRODUCTION	16
2 NORMAL AND ANOMALOUS DIFFUSION.....	18
2.1 Fick's Law and Self Diffusion	18
2.2 Random Walk Model and Single-File Diffusion.....	21
2.3 Deviations from Single-File Diffusion in Finite Systems.....	23
3 NMR AND PULSED FIELD GRADIENT DIFFUSOMETRY THEORY	25
3.1 Fundamentals of Nuclear Magnetic Resonance	25
3.1.1 Spin, Precession, and Magnetization	25
3.1.2 Longitudinal and Transverse Relaxation	28
3.1.3 NMR Spectroscopy.....	31
3.2 Pulsed Field Gradient NMR	31
3.2.1 Field Gradient.....	32
3.2.2 Spin Echo	32
3.2.3 PFG NMR Spin Echo Sequences.....	35
3.3 Experimental NMR Details.....	37
4 SINGLE-FILE DIFFUSION IN MIXTURES.....	40
4.1 Motivation	40
4.2 Review of Published Single-File Diffusion Studies.....	40
4.3 Sorbent and Sorbates Studied.....	42
4.4 Experimental Details	43
4.5 Observation of Single-File Diffusion in Mixtures	45
4.6 Summary	54
5 ABSENCE OF TRANSITION TO CENTER-OF-MASS DIFFUSION.....	55

5.1 Single-File Diffusion in Finite Systems.....	55
5.2 Relationship between Single-File Mobilities.....	58
5.3 Summary	60
6 METHODOLOGY DEVELOPMENT- CALIBRATION OF MAGIC ANGLE SPINNING PROBE FOR NMR DIFFUSOMETRY	62
6.1 Motivation	62
6.2 Gradient Calibration.....	63
6.3 Reference Measurement in Microporous Material	67
6.4 Summary	76
7 WORK IN PROGRESS: DIFFUSION IN THE PRESENCE OF HYDROGEN SULFIDE.....	78
7.1 Motivation	78
7.2 Diffusion of Hydrogen Sulfide	79
7.2.1 Experimental Details.....	79
7.2.2 Results and Discussion	80
7.3 Influence of Hydrogen Sulfide Exposure on Transport Properties	82
7.3.1 Experimental Details.....	83
7.3.2 Results and Discussion	85
7.4 Summary	87
8 CONCLUSIONS	94
LIST OF REFERENCES	97
BIOGRAPHICAL SKETCH.....	102

LIST OF TABLES

<u>Table</u>	<u>page</u>
4-1	Gas concentration (in mol/kg of AV) obtained for the studied samples using NMR signal analysis. 44
4-2	Single-File mobilities (F_{helix}) estimated from attenuation curves in Figure 4-1 and 4-2 using Eq 4-6. 51
5-1	Estimates of fractional loadings (θ), the values of MSD at which a transition from SFD to COM diffusion is predicted by Eq 5-1 ($z_{2\text{COM}}$), and the minimum cluster size required by Eq 5-1 for not observing this transition under the reported experimental conditions of this study. 57
6-1	Values of maximum gradient strength, g_1 (T/m), calculated using Eq 6-1 for two spacers of varying lengths. 65
6-2	Ensemble fractions and the corresponding diffusivities obtained by fitting Eq 6-1 to the bi-exponential attenuation curves in Figure 6-8. 74
7-1	Concentration (mmol/g) of C_2H_4 molecules adsorbed in pure and exposed ZIF-8 crystals as determined using NMR signal analysis. 90
7-2	The parameters corresponding to the bi-exponential curve fit to the T_1 relaxation data reported in Figure 7-4. 91
7-3	Parameters corresponding to the bi-exponential (Eq 6-1) and mono-exponential fits used to describe attenuation curves for both pure and exposed ZIF-8 at selected diffusion times. 92

LIST OF FIGURES

<u>Figure</u>	<u>page</u>
2-1 Illustration of measurement of diffusion.....	19
3-1 Precession of magnetic dipole moment in response to the application of a magnetic field in the z-direction is a function of the initial direction of the spin... 27	27
3-2 Schematic of a collection of nuclear spins at thermal equilibrium after being subjected to a magnetic field. The result is in a net macroscopic magnetization aligned along the direction of the magnetic field.	29
3-3 The transfer of the net magnetization from the z-axis to the -y-axis is possible with the application of a r.f. pulse. The transverse magnetization then continues to precess in the xy-plane.	30
3-4 Schematic illustration of the combined effect of a static, homogeneous magnetic field and a spatial dependent field gradient that results in a spatially dependent precession.	33
3-5 Schematic illustration of the three steps that describe all NMR diffusometry experiments.....	33
3-6 Schematic presentation of the spin echo based PFG NMR sequences	39
4-1 Schematic illustration of molecules restricted to move in a one-dimensional channel that has a radius smaller than the diameter of the molecules. Mutual passage is forbidden under these conditions.....	41
4-2 ¹³ C PFG NMR attenuation plots measured at 298 K for CO, CH ₄ , and CO ₂ diffusion in AV channels loaded with a single gas	49
4-3 ¹³ C PFG NMR attenuation plots measured for CO, CH ₄ , and CO ₂ diffusion as mixtures in AV channels at 298 K.....	50
4-4 MSD dependence on times plotted on a double-log scale.....	52
5-1 Illustration of difference in molecular motion in SFD and COM diffusion	56
6-1 A schematic of the MAS experimental setup combined with the pulsed field gradient coil, g(z), in a high-resolution MAS probe	63
6-2 The image profile acquired along the rotor axis for a mixture of H ₂ O/ D ₂ O at two gradient strengths	68
6-3 A plot of the NMR signal obtained at the smallest gradient strength normalized to the signal recorded at the largest gradient strength	68

6-4	The temperature dependence of sample temperature on the spin rate plotted as a function of the system temperature determined using neat methanol.....	69
6-5	Attenuation plots acquired using the MAS PFG NMR setup at various spin rates and diffusion times for a sample of water at 298 K	70
6-6	The ^1H NMR spectrum of non-activated ZIF-8 bed obtained using the high-resolution MAS probe	72
6-7	^1H spectrum obtained of H_2O molecules in a saturated ZIF-8 bed under conditions of MAS and static NMR	72
6-8	Overlay of the attenuating signal of H_2O saturated in the ZIF-8 bed resulting from increasing applied gradient.....	73
6-9	Measured PFG NMR attenuation curves for H_2O diffusion in a saturated ZIF-8 bed under MAS conditions with a spin rate of 5 kHz.	75
6-10	Attenuation curve obtained using deconvolution of overlapping peaks observed in the PFG NMR spectra of H_2O diffusion in ZIF-8.....	75
7-1	Schematic of transport on different length scales in a cross-section of a membrane.	78
7-2	The evolution of the peak identified as H_2S in ZIF-8 acquired using the 13-interval PFG NMR sequence	88
7-3	Example of ^1H spectra acquired of H_2S in ZIF-8 using the 14 T spectrometer and diff30 gradient probe.....	89
7-4	T_1 Relaxation curves obtained using ^{13}C NMR show a bi-exponential distribution	90
7-5	Examples of measured attenuation curves obtained using ^{13}C (black symbols) and ^1H (red symbols) PFG NMR of Ethylene diffusion at 298 K.....	91
7-6	SEM images provided by collaborators in Dr. Ryan Lively's group of pure and exposed ZIF-8.	93

LIST OF SYMBOLS

B_0	static magnetic field
c, c^*	molar concentration/of labeled particles
d	diameter of single-file AV channel
D, D^*	transport diffusivity/of labeled particles
$\mathcal{D}, \mathcal{D}_0, \mathcal{D}_{\text{COM}}$	self-diffusivity/of isolated particles/center-of-mass diffusivity
F, F_{helix}	single-file mobility/along the helical AV channel
g, g_i, g_a	Gradient
\hbar	planck's constant divided by 2π
J, J^*	molar transport flux/of labeled particles
l, l_i, l_j	elementary step of a particle/ i/j in the diffusion model
L	length of AV crystals
M_s	spin azimuthal quantum number
n	number of steps in the diffusion manual
N^*	total number of labeled molecules
p	geometrical factor relating true path length and helical path length
p_i	ensemble factions
P	probability distribution
$\langle r^2(t) \rangle$	mean-squared displacement
\vec{S}	angular spin momentum
S	spin quantum number
$S(g)$	signal intensity as a function of magnetic field
t	Time
T_1	longitudinal NMR relaxation constant

T_2	transverse NMR relaxation constant
$\langle z^2(t) \rangle$	one-dimensional mean-squared displacement
ε	length of spacer
γ	gyromagnetic ratio
θ	site occupancy
λ	length of elementary step in single-file diffusion manual
Ψ	attenuation
τ, τ	elementary time between each step in the diffusion model/single-file diffusion model
$\vec{\mu}$	magnetic dipole moment
ω	angular frequency

LIST OF ABBREVIATIONS

MSD	mean square displacement
MOF	metal organic framework
NMR	nuclear magnetic resonance
PFG NMR	pulsed field gradient nuclear magnetic resonance
PGSTE	pulsed gradient stimulated echo
PGSTEBP LED	pulsed gradient stimulated echo using bipolar gradients with longitudinal eddy-current delay
r.f.	Radiofrequency
SEM	scanning electron microscope
ZIF	zeolitic imidazolate framework

Abstract of Dissertation Presented to the Graduate School
of the University of Florida in Partial Fulfillment of the
Requirements for the Degree of Doctor of Philosophy

GAS DIFFUSION IN STRONGLY CONFINING AND INTERACTING MICROPOROUS
SORBENTS BY NMR

By

Akshita Ranjan Dutta

August 2017

Chair: Sergey Vasenkov
Cochair: Kirk. J. Ziegler
Major: Chemical Engineering

Gas separations is a process relevant to a variety of chemical industries ranging from petrochemicals and biofuels to pharmaceuticals. The importance of this process has inspired the development of novel materials and technology tailored for efficient membrane-based technologies. The main long-term goal of the work presented in this dissertation is to develop the fundamental science for a conceptually new type of gas separations which is based on induction of single-file diffusion (SFD) for a selected component of a gas mixture inside a microporous membrane. SFD can be exhibited by molecules confined in narrow unidimensional channels that prevent mutual molecular passages. The unique properties associated with this anomalous diffusion mechanism offer the possibility of highly-selective separations.

In this work a diffusion NMR technique at high magnetic field and high magnetic field gradient has enabled the first experimental observation of SFD of molecular mixtures and provided insight into the relationship between SFD rates of pure-sorbates and their respective mixtures. The studied gases include methane and carbon dioxide, which are relevant for natural gas separations. Molecular clustering in the investigated

model single-file channels is proposed to explain the observed relationship between the mixture and one-component mobilities and to reconcile reported experimental data with predictions of a random walk model.

In addition to carbon dioxide, hydrogen sulfide represents another hazardous impurity in natural gas. Zeolitic imidazolate frameworks (ZIFs) are promising candidates for natural gas separation and processing. Diffusion NMR was applied to study dynamics of hydrogen sulfide in ZIF-8. Preliminary results reveal an extremely low mobility of hydrogen sulfide in this material. Investigation of the influence of hydrogen sulfide exposure on the transport properties of ZIF-8 is currently underway.

NMR diffusometry is a powerful technique for studying diffusion phenomena in porous materials. However, short NMR transverse relaxation times under conditions of extreme confinement in microporous materials limit applicability of standard diffusion NMR. In an effort to overcome this challenge, a NMR probe capable of performing diffusion measurements under magic angle spinning (MAS) was calibrated and applied for diffusion studies in ZIFs. These studies demonstrate that MAS can drastically improve conditions of NMR diffusion measurements.

CHAPTER 1 INTRODUCTION

Separation processes account for 10-15% of our nation's energy consumption due to the high-energy cost associated with thermally driven processes such as distillation, drying, and evaporation.¹⁻² Low-energy separation processes like membrane-based separations are both economically and environmentally friendly alternatives. Universal implementation of membrane technology is currently hindered by barriers that limit their potential.³ Progress on this front requires advancements in process innovation as well as development of novel materials. In this dissertation, both these approaches are acknowledged.

Highly-selective membrane-based separations are challenging because they demand stringent control and uniform distribution of pore sizes.⁴ These porous materials must then be tailored and customized for a given separation.⁵⁻⁶ A conceptually new type of separation based on induction of single-file diffusion can relieve some of these requirements. Single-file channels forbid molecules inside the channels from passing each other during a diffusion process by geometrically constraining them and, hence, conserving their relative order in the channels. This correlated movement manifests as unique properties that can be exploited to achieve effective separations. Incorporating this diffusion mechanism in applications requires a fundamental understanding of single-file diffusion of mixtures. While there have been numerous theoretical and simulation studies on mixtures confined to single-file channels, there have been no previous experimental reports on it.

In Chapter 4 the first experimental observation of single-file diffusion of mixtures is presented. CO, CO₂, and CH₄ gas molecules confined under single-file conditions in

L-Ala-L-Val nanochannels as both pure and binary mixtures is investigated using pulsed field gradient (PFG) NMR at the high field of 17.6 T. The unique relationship between single-file mobilities of the sorbates in pure and mixture form is also discussed. Chapter 5 presents a comparison of theoretical predictions and the reported experimental trends of single-file diffusion of mixtures in finite systems. This comparison drives the discussion of the presence of molecular clusters in the studied pure and mixture samples.

Complementary to the investigation of the fundamental science of a unique transport phenomenon, microscopic diffusion studies in existing sorbents is the focus of Chapters 6 and 7. Novel, microporous materials are often introduced and reported in literature as promising materials for challenging and industrially important membrane-based separations. To identify and characterize the potential of such materials, a thorough understanding of diffusion on a microscopic scale is essential. The development of a new methodology that can expand the range of microporous systems that can be studied in this manner is presented in Chapter 6. Chapter 7 reports the study of microscopic diffusion in the presence of a toxic and hazardous gas, hydrogen sulfide. The possible presence of strong interactions between the framework of the porous material and hydrogen sulfide is revealed here. In addition, the influence of exposure to this corrosive gas on the transport properties of the sorbent is being investigated.

In the next two chapters, Chapters 2 and 3, the theory of diffusion, NMR spectroscopy, and NMR diffusometry is presented.

CHAPTER 2 NORMAL AND ANOMALOUS DIFFUSION

Diffusion is the process of migration of molecules tending towards elimination of spatial variations and is driven by non-zero internal energy of systems at temperatures above absolute zero.⁷⁻⁸ It is a manifestation of the tendency of matter to approach maximum entropy.⁹ This is a fundamental transport phenomenon that has been studied since the 19th century.

2.1 Fick's Law and Self Diffusion

Adolf Fick introduced two laws that describe macroscopic diffusion by studying the rate of interdiffusion of two gases, at constant pressure. Fick's first law of diffusion is given by:

$$J = -D \frac{\partial c}{\partial z} \quad (2-1)$$

where J is the molar flux, D is the diffusivity, c is the concentration, and z is the spatial coordinate.⁸ The molar flux is defined as the net number of molecules that flow in the z direction per unit area normal to this direction, per unit of time. Fick's first law can be used to define the diffusive flux of a species, and according to Eq 2-1, it opposes the concentration gradient of the species. The diffusivity, D, generally implies the diffusivity of a species in a given medium such as another solvent, a biological membrane, or microporous materials, which are studied in this work.

For diffusion in one-dimension, as described in Eq 2-1, provided that diffusivity is independent of concentration, Fick's second law is:

$$\frac{\partial c}{\partial t} = -D \frac{\partial^2 c}{\partial z^2} \quad (2-2)$$

and is a consequence of the application of the conservation of mass principle.

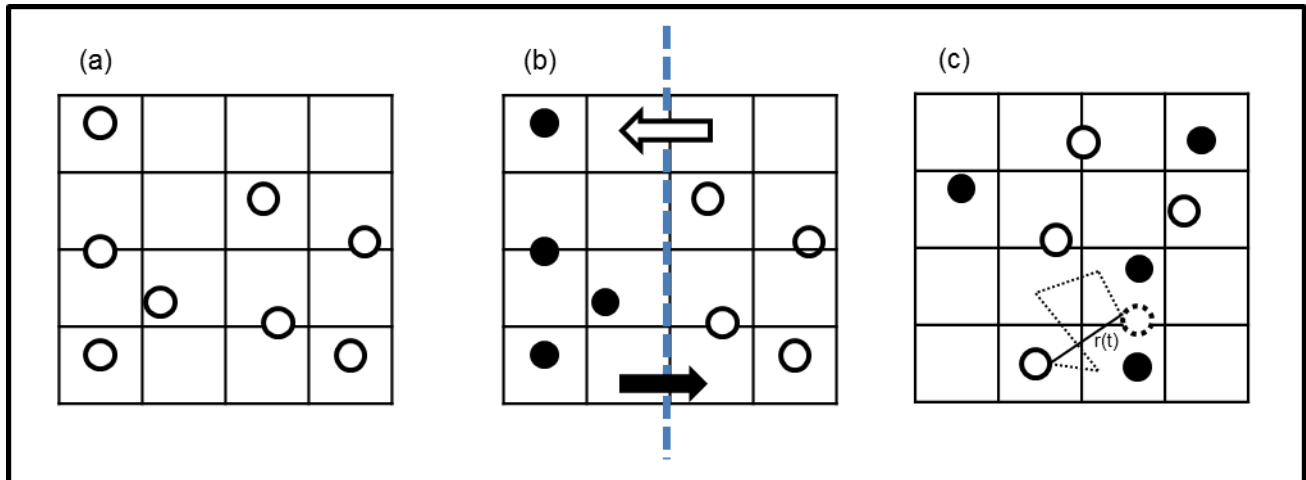


Figure 2-1. Measurement of self-diffusion in an (a) equilibrated system is illustrated here by (b) labeling (●) half of the molecules and tracking their flux or (c) displacements of each molecule.

Brownian motion is the molecular movement under conditions of macroscopic equilibrium. It is driven by thermal fluctuations, resulting in random displacements of molecules. In the absence of a macroscopic concentration gradient, the diffusivity is classified as self-diffusivity (\mathcal{D}).

The connection between Fick's laws and Brownian molecular motion was established by Einstein.¹⁰ Figure 2-1 illustrates this connection by invoking a concentration gradient in an initially equilibrated system through "labeling" of exactly half the molecules.¹¹ The system is then allowed to come to equilibrium as shown in Figure 2-1 (c). In analogy to Eq 2-1, the self-diffusivity can be defined in terms of the flux, J^* , and concentration, c^* , of labeled molecules by:

$$J^* = -D^* \frac{\partial c^*}{\partial z} \quad (2-3)$$

under the constraint that total concentration of molecules is constant. Since the flux of labeled molecules is equal in magnitude but opposite in direction to unlabeled molecules, and their concentrations are equal, the diffusivities of both labeled and

unlabeled are identical and defined as the self-diffusion coefficient, \mathcal{D} . Hence, it follows, that Fick's second law for this system of labeled molecules in a one-dimensional coordinate system is:

$$\frac{\partial c^*}{\partial t} = -\mathcal{D} \frac{\partial^2 c^*}{\partial z^2} \quad (2-4)$$

where the total concentration of molecules remains constant. For the initial condition that the labeled species are confined at $z=0$, the solution to Eq 2-4 has the form:

$$c^* = \frac{A}{\sqrt{t}} \exp\left(-\frac{z^2}{4\mathcal{D}t}\right) \quad (2-5)$$

where A is a constant. The total number of molecules, N^* , is preserved and can be determined by integrating over the infinite length in the z direction by:

$$N^* = \int_{-\infty}^{\infty} c^* dz = \int_{-\infty}^{\infty} \frac{A}{\sqrt{t}} \exp\left(-\frac{z^2}{4\mathcal{D}t}\right) dz = 2A\sqrt{\mathcal{D}} \pi \quad (2-6)$$

The resulting solution for isotropic diffusion from a point source is derived by combining Eq 2-5 and 2-6:

$$\frac{c^*}{N^*} = \frac{1}{\sqrt{4\pi\mathcal{D}t}} \exp\left(-\frac{z^2}{4\mathcal{D}t}\right) \quad (2-7)$$

and is termed the diffusion "propagator".

The mean square displacement (MSD) of the labeled molecules after time t can be calculated by integration:

$$\langle z^2(t) \rangle = \int_{-\infty}^{\infty} \frac{z^2}{\sqrt{4\pi\mathcal{D}t}} \exp\left(-\frac{z^2}{4\mathcal{D}t}\right) dz = 2\mathcal{D}t \quad (2-8)$$

Equation 2-8 is generally known as Einstein's equation and provides a direct correlation between the self-diffusivity as defined by Fick's first law in Eq 2-4 and an experimentally observable relation, the MSD dependence on time.

Synonymously, the propagator for a molecule initially located at the origin and allowed to occupy three-dimensional space can be derived and the corresponding MSD relation to time is:

$$\langle r^2(t) \rangle = 6Dt \quad (2-9)$$

where r is the final position of the molecule.

2.2 Random Walk Model and Single-File Diffusion

An alternative approach to understand self-diffusion, both qualitatively and quantitatively, is the random-walk model. The random walk is a sequence of steps a particle can take in any direction with equal probability and at constant frequency, given that each step is of equal length.¹² This section outlines the random walk model for a particle allowed to move in one-dimension. It also extends the model to more complex systems that give rise to non-random correlations between successive steps.

A single particle in a one-dimensional system takes steps of ± 1 with equal probability, allowing for time, τ , between each step. In this scenario, the mean square distance traveled by the particle after n steps, is given by:

$$\langle z^2(n) \rangle = \left\langle \left(\sum_{i=1}^n l_i \right)^2 \right\rangle = \sum_{i=1}^n \langle l_i^2 \rangle + \sum_{i \neq j} \langle l_i l_j \rangle \quad (2-10)$$

Assuming the direction of a given step is uncorrelated to the previous step, the term $\langle l_i l_j \rangle$ in Eq 2-10 can be rewritten as $\langle l_i \rangle \langle l_j \rangle$ where $\langle l_i \rangle = 0$. Hence, Eq 2-10 simplifies to:⁶

$$\langle z^2(n) \rangle = nl^2 \quad (2-11)$$

The relationship between the number of steps and time is given by $t = n\tau$ which when substituted in Eq 2-11 gives:

$$\langle z^2(t) \rangle = 2Dt \quad (2-12)$$

where $D = l^2/2\tau$. The corresponding probability distribution of displacements for a particle subjected to a one-dimensional random walk is:¹²

$$P(z,t) = \frac{1}{\sqrt{4\pi Dt}} \exp\left(-\frac{z^2}{4Dt}\right) \quad (2-13)$$

It should be noted that this probability distribution is equivalent to the diffusion “propagator” of labeled particles presented in Eq 2-7. Both these expressions (Eq 2-7 and Eq 2-13) describe the normal self-diffusion process.

The foundation for the mathematical description of normal diffusion is the concept of uncorrelated movements of molecules. A system, in which particles are confined to move in one-dimensional channels so narrow that their mutual passage is forbidden, deviates from the features of normal diffusion. Here, the order of molecules is preserved. This specific anomalous diffusion mechanism is known as single-file diffusion (SFD).

The correlated motion of particles in single-file system can be examined in the context of the MSD expression describing a random walker in one-dimension (Eq 2-10), where the term $\sum_{i \neq j} \langle l_i l_j \rangle$ is negative. This is because under single-file confinement, a particle can attempt to step in either direction with equal probability but can only move successfully if directed to a vacant site.⁶ The corresponding MSD dependence on time is given by:

$$\langle z^2(t) \rangle = 2Ft^{1/2} \quad (2-14)$$

where F is the single-file mobility factor. The growth of MSD with the square root of time is a unique signature of SFD. The single-file mobility factor, F , is a function of site

occupancy, θ , the mean time between each step, τ , and the length of each step, λ , as described by the following equation:¹²

$$F = \lambda^2 \left(\frac{1-\theta}{\theta} \right) \frac{1}{\sqrt{2\pi\tau}} \quad (2-15)$$

The diffusion propagator for single-file diffusion, as for normal diffusion, is a Gaussian function. The relationship between the mobility factor, F , of a particle in a single-file system and its self-diffusivity, \mathcal{D}_0 , as a sole particle in this system is:

$$F = \lambda \left(\frac{1-\theta}{\theta} \right) \sqrt{\frac{\mathcal{D}_0}{\pi}} \quad (2-16)$$

It should be noted that, Equation 2-14 is only valid for sufficiently large observation times, such that the particles become “aware” of their neighbors.¹²

2.3 Deviations from Single-File Diffusion in Finite Systems

In finite, single-file channels, with fast molecular exchange at boundaries, a transition to the time scaling of MSD for normal diffusion is predicted by theoretical and mathematical models. This behavior is understood by considering a selected time interval in which a particle enters the channel at one end while another exits at the opposite end. The coincidence of these events results in a shift in the chain of molecules that occupy the channel, by one position. However, this shift in the chain of molecules at a given moment is uncorrelated with the previous one which is a distinct feature of normal diffusion. This form of molecular propagation is known as center-of-mass (COM) diffusion.¹³⁻¹⁴ The MSD dependence on time in this diffusion regime can be summarized by Einstein’s relation (Eq 2-8), where the effective diffusivity, \mathcal{D}_{COM} , can be described as follows:

$$\mathcal{D}_{\text{COM}} = \mathcal{D}_0 \left(\frac{1-\theta}{\theta} \right) \frac{\lambda}{L} \quad (2-17)$$

in terms of the diffusivity of an isolated particle in the single-file channel, \mathcal{D}_0 , the site occupancy, θ , the channel length, L , and the elementary step of a particle, λ .¹⁵

Over sufficiently long observation times, in a finite single-file channel with “open” boundaries that allow for molecular exchange, center-of-mass diffusion becomes the dominating mode of transport. The MSD at which a transition from SFD to COM diffusion is expected is described by the parameters listed in Eq 2-17:¹⁵

$$\langle z^2 \rangle_{\text{COM}} = \left(\frac{1-\theta}{\theta} \right) \frac{2L\lambda}{\pi} \quad (2-18)$$

The case of reflecting boundaries would also result in deviations but towards smaller displacements. Since motion in finite, single-file channels is sensitive to boundary conditions observation of SFD can be a challenge.¹²

CHAPTER 3 NMR AND PULSED FIELD GRADIENT DIFFUSOMETRY THEORY

Nuclear magnetic resonance (NMR) is an experimental technique that exploits the interaction between certain atomic nuclei and resonant radio-frequency (RF) radiation in the presence of an external magnetic field to gain molecular information. The atomic nuclei that are sensitive to this analytical technique must have a non-zero magnetic moment. This non-invasive technique has wide applications ranging from imaging of biological subjects to determination of complex molecular structures. The work presented here is based on an NMR diffusometry method called Pulsed Field Gradient (PFG) NMR, which is used to study both normal and anomalous diffusion in microporous materials. This chapter provides a brief overview of the fundamentals of NMR and PFG NMR.

3.1 Fundamentals of Nuclear Magnetic Resonance

3.1.1 Spin, Precession, and Magnetization

Spin is an intrinsic quantum mechanical property of elementary particles.¹⁶ Each of these particles has a spin quantum number, S , associated with it. It is described to be a form of angular momentum that a particle possesses. In quantum mechanics, the angular momentum is quantized and the total angular momentum, \vec{S} , of a particle with spin takes a value of $[S(S+1)]^{1/2}\hbar$, where \hbar is Planck's constant divided by 2π . A total of $2S+1$ spin sublevels exist, that are described by the azimuthal quantum number, M_s .¹⁷ This quantum number can take on specific values between $-S$ and S . In the absence of a magnetic field, all $2S+1$ states for a given value of S are degenerate. The introduction of a magnetic field can break this degeneracy.

Since nuclei are made up of elementary particles that have spin, consequently, they too have a spin (l) and azimuthal (m) quantum number associated with them. The relationship between these numbers and the information provided by them is analogous to that for particle spin quantum numbers described above. While the quantum mechanical perspective of spins is described thus far, for the sake of clarity the following discussion will be based on semi-classical approach.

Fundamental particles and, hence, atomic nuclei also have an intrinsic magnetic dipole moment, $\vec{\mu}$, that is closely related to the spin angular momentum, \vec{S} , by

$$\vec{\mu} = \gamma \vec{S} \quad (3-1)$$

where γ is a proportionality constant known as the gyromagnetic ratio.¹⁷ The direction of spin angular momentum, known as polarization spin axis, can point in any possible direction, in complete analogy to the angular momentum of a rotating object. In the presence of an external magnetic field, \vec{B} , the response of the polarization is to move around the magnetic field. This motion is physically described to result from a torque, $\vec{\tau}$, that is applied to the atomic spin as given by:¹⁸

$$\vec{\tau} = \vec{\mu} \times \vec{B} \quad (3-2)$$

Torque is the time derivative of angular momentum, leading to the following relationship:

$$\vec{\tau} = \frac{d\vec{S}}{dt} = \frac{1}{\gamma} \frac{d\vec{\mu}}{dt} = \vec{\mu} \times \vec{B} \quad (3-3)$$

Traditionally in NMR the applied magnetic field is aligned along the z-direction such that $\vec{B}=(0,0,B_0)$. Combining this with the cross product shown in Eq 3-3 reveals the time-evolution of the magnetic dipole moment in each Cartesian component as a function of

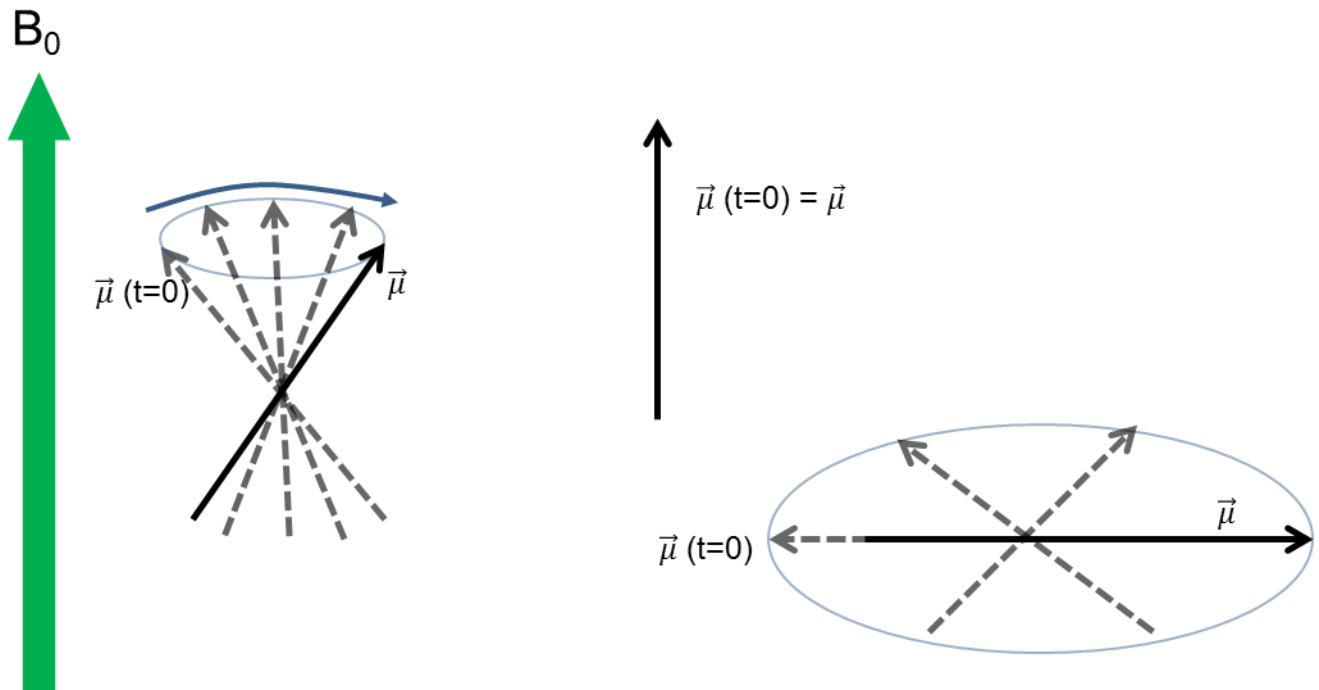


Figure 3-1. Precession of magnetic dipole moment in response to the application of a magnetic field in the z-direction is a function of the initial direction of the spin.

its direction before application of the magnetic field. If visualized, the magnetic moment moves on a cone, maintaining a constant angle between itself and the field as shown in Figure 3-1. This motion is called precession and a quantum treatment of it shows that the frequency of precession, ω_0 , is given by:

$$\omega_0 = -\gamma B_0 \quad (3-4)$$

where γ is the gyromagnetic ratio and B_0 is the magnetic field applied Eq 3-4 also applies to nuclear spins for which the angular frequency is termed Larmor frequency.

The energy of a magnetic dipole, E , in the presence of a magnetic field is given by:

$$E = -\vec{\mu} \cdot \vec{B} \quad (3-5)$$

This energy depends on the relative direction of the magnetic dipole and magnetic field vectors. As mentioned earlier, a magnetic field, B_0 , applied in the z-direction, simplifies

Eq 3-5 to show that each spin state will have a distinct energy level, an effect known as Zeeman splitting:

$$E = -\gamma S_z B_0 = -M_s \hbar \gamma B_0 \quad (3-6)$$

Equation 3-5 indicates that the magnetic energy is lowest if the magnetic moment is parallel to the magnetic field. The Boltzmann distribution describes the population distribution of the spin states to a good approximation.⁹ Accordingly, the population of nuclear spins in the lowest energy state is higher than in the higher energy state.

In NMR spectroscopy, a macroscopic ensemble of molecules is generally observed. The application of a magnetic field to a large sample of nuclear spins results in a magnetization vector, \vec{M} , that is the sum of all nuclear dipole moments:

$$\vec{M} = \sum_j \vec{\mu}_j \quad (3-7)$$

The net magnetization is in the direction parallel to \vec{B} and arises from the relative difference in population of spins at different energy states. Since the energy is not dependent on the x and y components, the vector sum of the nuclear dipole moments along these coordinates is zero. Hence, at thermal equilibrium, the magnetization is M_{eq} aligned along the z-direction, as visualized in Figure 3-2.

3.1.2 Longitudinal and Transverse Relaxation

“Relaxation” is a term widely used to refer to the re-establishment of thermal equilibrium after application of a perturbation. In NMR studies, before the introduction of a magnetic field, the system is in equilibrium in a state where all spins orientations are equally probable. Once a magnetic field is applied, the system “relaxes” to a new equilibrium state shown in Figure 3-2. The time it takes for magnetization to reach this latter state is dictated by the time constant, T_1 , also known as the longitudinal relaxation

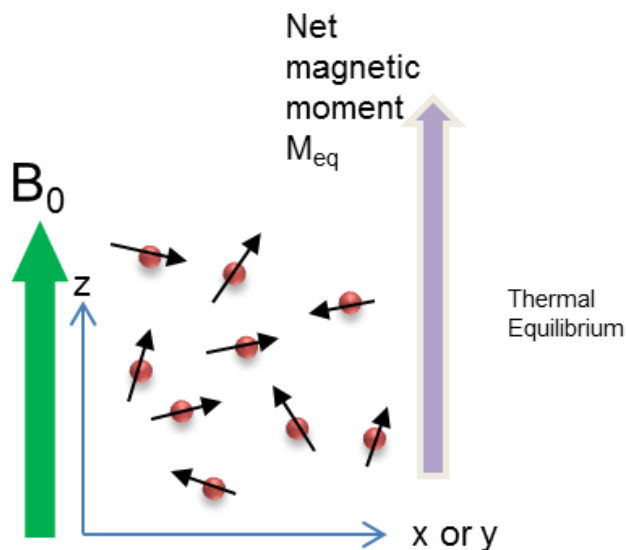


Figure 3-2. Schematic of a collection of nuclear spins at thermal equilibrium after being subjected to a magnetic field. The result is in a net macroscopic magnetization aligned along the direction of the magnetic field.

time constant. The build-up of this magnetization is described by the following equation:

$$M_z(t) = M_{eq} \left(1 - \exp\left(-\frac{t}{T_1}\right) \right) \quad (3-8)$$

The relaxation constant T_1 is a function of the sample and the nuclear isotope. It can range from seconds to even days in exceptional cases.

The magnitude of the magnetization M_{eq} is almost undetectable, making experimental study of this magnetization impractical. There is no net magnetization in the x-y plane as discussed in the previous section. To measure the magnetization that does exist along the z-axis, the polarization of every single spin can be rotated by $\pi/2$ radians around the x-axis by applying the appropriate radiofrequency (r.f.) pulse. Accordingly, the net polarization along the z-axis is transferred to align with the -y-axis. Transverse magnetization refers to this net magnetic moment perpendicular to the magnetic field direction. Once the r.f. pulse is turned off, every single spin begins to

precess, and hence the net magnetic moment also precesses. Figure 3-3 is a schematic demonstrating this motion.

The microscopic field experienced by these spins fluctuates over time, causing their precession frequency to vary. This causes the precessing nuclear spins that make up the net magnetic moment to get out of phase with each other. The result is an irreversible decay of the transverse magnetization. The time constant, T_2 , dictates the time it takes for this magnetization to decay. It is referred to as the transverse relaxation time. The time evolution of the components of the net magnetization after the r.f. pulse is removed is described by:

$$M_y = -M_{eq} \cos(-\gamma B_0 t) \exp\left(-\frac{t}{T_2}\right) \quad (3-9)$$

$$M_x = M_{eq} \sin(-\gamma B_0 t) \exp\left(-\frac{t}{T_2}\right) \quad (3-10)$$

The value of T_2 also depends on the system being studied. For small molecules in liquids, it is on the same order of magnitude as the T_1 relaxation time. For gas molecules in porous materials, it can be as short as a few milliseconds.

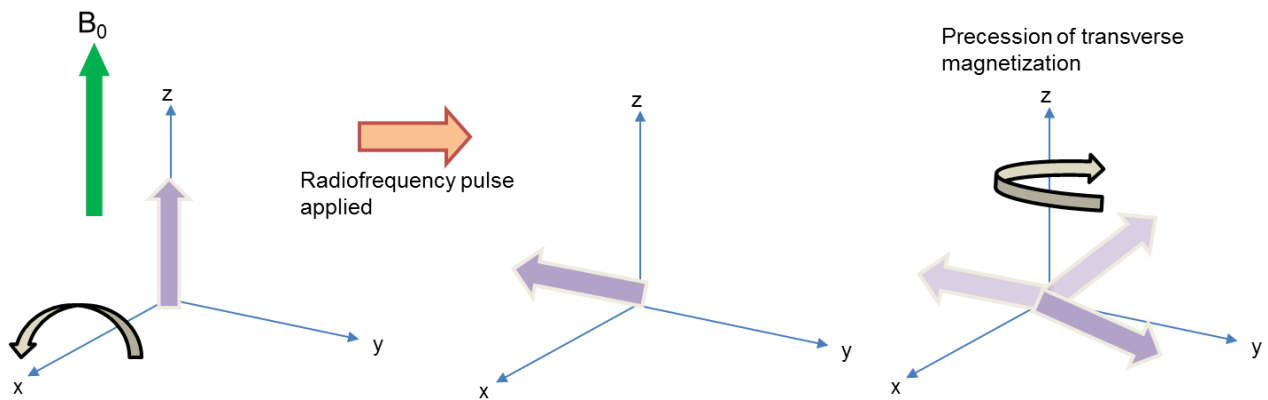


Figure 3-3. The transfer of the net magnetization from the z-axis to the -y-axis is possible with the application of a r.f. pulse. The transverse magnetization then continues to precess in the xy-plane.

3.1.3 NMR Spectroscopy

The transverse magnetization is detectable as it oscillates at a well-defined frequency (Eq 3-9 and Eq 3-10). The rotation of the magnetic moment produces a rotating magnetic field. Based on Maxwell's equations, a changing magnetic field is related to an electric field which can generate an electric current if a coil is introduced perpendicular to the transverse plane. The resulting oscillating current is called the free-induction decay (FID).

To briefly summarize, the NMR spectrometer is capable of: (i) applying a large magnetic field to produce a net magnetization; (ii) applying r.f. pulses to rotate the spin polarization into the transverse plane; (iii) detecting the electric current generated by the precessing transverse magnetization. The frequency and duration of the r.f. pulse influences the degree of rotation of the net magnetization. Hence, the application of a resonant r.f. pulse can rotate the net magnetization between the longitudinal and transverse plane.

3.2 Pulsed Field Gradient NMR

Pulsed Field Gradient (PFG) NMR, an application of NMR, is able to trace molecular displacements on the order of 0.1 μm to hundreds of micrometers by determining the mean propagator for displacements. It is a powerful technique to investigate diffusion in nanoporous and microporous systems as it can distinguish between various features of mass transfer such as intra-crystalline diffusion, permeation of surface resistances, and long-range diffusion.¹² PFG NMR measurements are performed under conditions where there is no significant convective flow and there is a uniform macroscopic chemical potential throughout the sample. Hence, the

measurements conducted are of self-diffusion of a given sorbate. The following sections elaborate on the fundamentals of PFG NMR as well as the type of measurements.

3.2.1 Field Gradient

PFG NMR is a technique that is based on creating an inhomogeneous magnetic field B_{eff} that varies with position. This is achieved by the superposition of a magnetic field, gz , that depends on position onto the constant field, B_0 :

$$B_{\text{eff}} = B_0 + gz \quad (3-11)$$

where the field gradient, g , is applied along the z -direction. The consequence of the application of the position dependent field gradient is the spatial dependence of the Larmor frequency of nuclei. The resulting effective Larmor frequency, ω_{eff} , is given by:

$$\omega_{\text{eff}} = -\gamma(B_0 + gz) \quad (3-12)$$

Figure 3-4 is a schematic illustration of the effect of the effective B_{eff} on the effective Larmor frequency, ω_{eff} .

The phase angle $\phi(t)$ accumulated by the nuclear spins as a result of their precession motion during the application of the field gradient pulse applied for a time, δ is described by Eq 3-13:

$$\phi(t) = -\gamma \int_0^{\delta} B_0 + gz(t') dt' \quad (3-13)$$

The average of positions of nuclear spins, as recorded by the angular phase, $\phi(t)$, becomes accessible through the NMR signal.

3.2.2 Spin Echo

The measurements of diffusion based on PFG NMR technique are based on the application of two field gradients applied over short time intervals. Hence, this yields the difference in location of molecules during these gradient pulses. Figure 3-5 illustrates

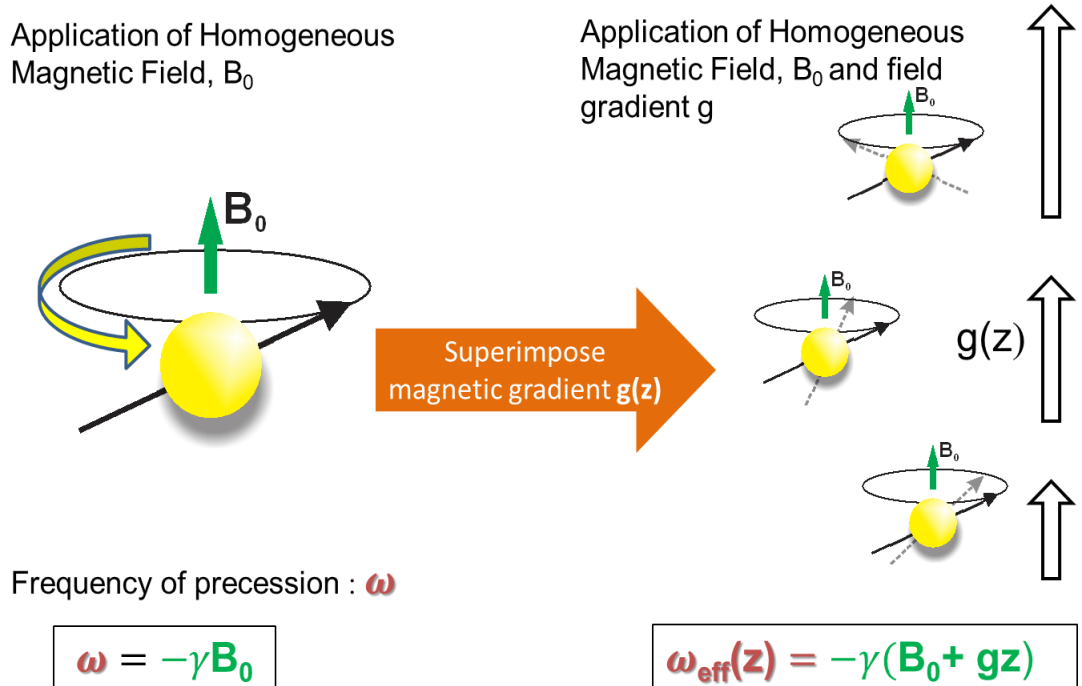


Figure 3-4. Schematic illustration of the combined effect of a static, homogeneous magnetic field and a spatial dependent field gradient that results in a spatially dependent precession.

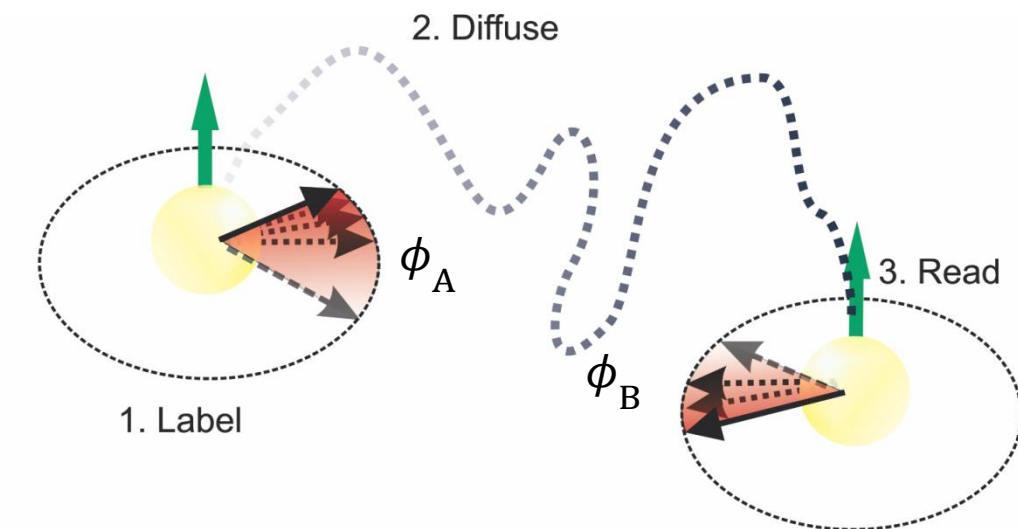


Figure 3-5. Schematic illustration of the three steps that describe all NMR diffusometry experiments that involve the application of two gradients of equal magnitude and duration but opposite sign and separated by a certain time delay allowed for diffusion.

the three general components of all NMR based diffusometry experiments: (i) labeling the initial position during the application of the first field gradient; (ii) a time delay that allows molecules to diffuse to a new position; (iii) reading the final position by means of the second field gradient that is equal in magnitude and duration but opposite in sign to the that employed in (i).

In practice, PFG NMR sequences are based on the spin echo experiment. As previously discussed, a $\pi/2$ r.f. pulse is initially applied to rotate net magnetization arising from the presence of homogeneous magnetic field, B_0 , into the transverse plane. The application of a gradient field then causes a distribution of the precession frequencies which translates to a reduction in the observed magnetization vector, which is determined by the distribution of phase angles. The implementation of a π r.f. pulse following the first gradient inverts the accumulated phase. For example, if a phase ϕ_A is acquired during time, τ , in which the field gradient was present, it is inverted to $-\phi_A$ with the application of the π r.f. pulse. Following a duration τ after the second r.f. pulse, the spins continue to precess and accumulate an additional phase ϕ_B in the presence of the gradient field. In the absence of translational diffusion and transverse relaxation, there is no phase difference acquired between the two τ intervals, resulting in the acquisition of maximum magnetization. In reality, however, the phase accumulation in these two intervals is distinct due to self-diffusion of molecules as well as fluctuations in the microscopic field. Subsequently, the maximum amplitude of the spin echo decreases with time.

While the measurement of the magnitude of transverse magnetization after a spin echo can reveal information about self-diffusion and transverse relaxation, it is

limited in its utility for studying more complex systems such as porous materials.

However, the concept of spin echo is employed in other PFG NMR sequences that are traditionally used for such experiments, as outlined in the next section.

3.2.3 PFG NMR Spin Echo Sequences

Stejskal and Tanner introduced the first PFG NMR pulse sequence known as the pulsed gradient spin echo (PGSE) pulse sequence.¹⁹ In this sequence, the gradient field is pulsed for short intervals, δ , during the time interval, τ , between r.f. pulses. Figure 3-6 (a) presents a schematic of this sequence. As presented in the discussion of spin echoes, the application of the gradient pulses results in accumulation of spatially dependent phases which can be related to measured transverse magnetization, M_{xy} , by the following expression:¹⁹

$$M_{xy} = M_{eq} \exp\left(-\frac{2\tau}{T_2}\right) \exp\left(-\mathcal{D}(\gamma g \delta)^2 \left(\Delta - \frac{\delta}{3}\right)\right) \quad (3-14)$$

where M_{eq} is magnetization at thermal equilibrium, τ , Δ , and δ , are time intervals as labeled in Figure 3-6 (a). The self-diffusion process can be studied by altering the experimental parameters g , Δ , and δ while keeping τ constant and measuring the transverse magnetization. Keeping τ consistent eliminates the additional varying decay caused by T_2 relaxation effects with changing time.

More sophisticated pulse sequences have appeared in the study of self-diffusion using PFG NMR since the introduction of PGSE. Tanner published a new sequence known as the pulsed gradient stimulated echo (PGSTE) sequence that has greater utility in the field of transport in porous materials.²⁰ The PGSTE sequence is useful for cases where T_2 is much shorter than T_1 , as is often true for molecules in microporous

materials. A schematic presentation of the pulse sequence is shown in Figure 3-6 (b). PGSTE is a modification of PGSE where the π r.f. pulse is divided into two $\pi/2$ r.f. pulses. These new consecutive pulses share the same r.f. phase and are separated by a time interval equal to $\Delta - \tau_{ST}$. During this time interval, the magnetization is stored in the longitudinal direction. Along this axis, the nuclei relax as per the T_1 relaxation time constant allowing for much longer diffusion times as compared to τ in the PGSE sequence. The expected transverse magnetization based on the pulse sequence parameters presented in Figure 3-6 (b) are as follows:

$$M_{xy} = M_{eq} \left(\frac{1}{2} \right) \exp\left(-\frac{2\tau_{ST}}{T_2}\right) \exp\left(-\frac{\Delta - \tau_{ST}}{T_1}\right) \exp\left(-\mathcal{D}(\gamma g \delta)^2 \left(\Delta - \frac{\delta}{3}\right)\right) \quad (3-15)$$

Any additional unwanted magnetization in the transverse plane between the application of the 2nd and 3rd $\pi/2$ r.f. pulses can be removed with the introduction of an additional gradient pulse known as the spoiler gradient.

Heterogeneous materials, such as microporous materials can create internal gradients which arise from interfaces created by surfaces of varying magnetic susceptibilities. The presence of internal gradients has unintended effects on the magnetic field and can manifest as distortions leading to misleading measured attenuation. To minimize these effects, Cotts et al. proposed the 13-interval sequence also known as the pulsed field gradient stimulated echo bipolar sequence (PGSTEBP).²¹

Figure 3-6 (c) is schematic of the 13-interval sequence which employs gradients of opposing polarity. The effects of internal gradients are hence refocused after the second τ_{BP} interval. The relationship between the transverse magnetization and the experimental parameters is predicted by Eq 3-16:

$$M_{xy} = M_{eq} \left(\frac{1}{2} \right) \exp \left(-\frac{4\tau_{BP}}{T_2} \right) \exp \left(-\frac{\Delta - 2\tau_{BP}}{T_1} \right) \exp \left(-\mathcal{D}(2\gamma g \delta)^2 \left(\Delta - \frac{\delta}{6} - \frac{\tau_{BP}}{2} \right) \right) \quad (3-16)$$

3.3 Experimental NMR Details

The NMR experiments presented in this dissertation were performed at the Advanced Magnetic Resonance Imaging and Spectroscopy Facility of the National High Magnetic Field Laboratory, located at the University of Florida. Two Bruker Biospin spectrometers, 17.6 T and 14 T, were used for all measurements discussed. Magnetic field gradients were generated by diff60 and diff30 diffusion probes that are capable of producing gradients of amplitude as large as 30 T/m and 18 T/m, respectively. ^{13}C and ^1H nuclei were probed based on the nature of the sorbate and sorbent being studied.

The use of high magnetic field afforded enhanced NMR sensitivity. In particular, in the reported ^{13}C NMR studies, using high field offered vast improvements in signal-to-noise ratio of measured NMR signals. The focus of this work is on sorbents that have a strong influence on the sorbate dynamics being measured, either through confinement or interaction. Hence, the use of high field gradients offered the possibility to measure very small displacements, in the range of 100s nm to 10 μm , and perform measurements of very slowly diffusing molecules. Application of large gradients also allows performing measurements under conditions of short T_2 relaxation times because, in this case, even short gradients can result in large signal attenuations.

Diffusion measurements were carried out using the 13-interval or PFGSTEBP pulse sequence due to its resilience towards potential artefacts produced by the samples of interest in this work. In all cases, unless otherwise specified, the pulse sequence included a longitudinal eddy current delay (LED). During this additional time interval, magnetization is stored along the longitudinal axis as any additional eddy-

currents induced in the gradient coil decay. In addition, spoiler gradients and phase cycling were employed to minimize any distortions in the NMR signal and in turn increasing the reliability of the results.

Measured attenuation curves were used to acquire the self-diffusion data for all samples. Attenuation (Ψ) is defined as the PFG NMR signal obtained with the application of gradient strength, $g(z)$, normalized to the signal obtained with the application of the smallest gradient possible, $g(z) \approx 0$. All other experimental parameters of the pulse sequence are kept constant as the amplitude of the gradient is altered. The NMR signal recorded is obtained by integrating the area under the peak belonging to the sorbate of interest.

While the relationship between the attenuation of signal and the experimental parameters depends on the diffusion mechanism, certain parameters are consistent. Under the conditions that allow normal self-diffusion of multiple molecular n ensembles that exhibit distinct effective diffusivities the diffusion-induced signal attenuation can be predicted by the following attenuation equation:

$$\Psi = \frac{S(g)}{S(g \approx 0)} = \sum_{i=1}^n p_i \exp[-q^2 t \mathcal{D}_i] \quad (3-17)$$

where p_i and \mathcal{D}_i are the population fraction and self-diffusivity, respectively, of ensemble i . The factors q and t are calculated by the following equations:

$$q \equiv 2\gamma g \delta \quad (3-18)$$

$$t \equiv \Delta - \frac{\tau_{BP}}{2} - \frac{\delta}{6} \quad (3-19)$$

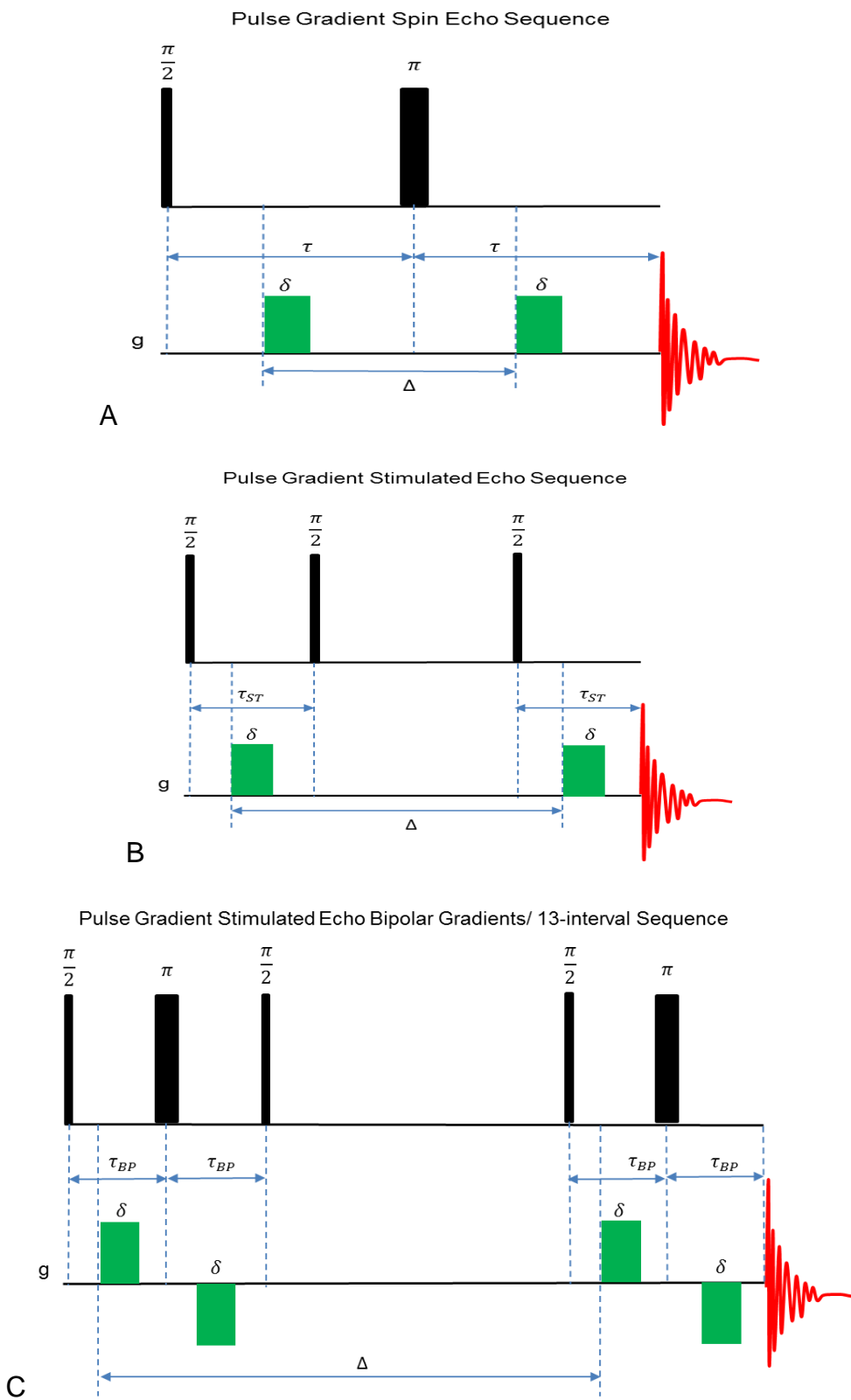


Figure 3-6. Schematic presentation of the spin echo based PFG NMR sequences: (A) PGSE, (B) PGSTE, and (C) PGSTEBP or 13-interval

CHAPTER 4 SINGLE-FILE DIFFUSION IN MIXTURES

4.1 Motivation

Molecules restricted to diffuse through unidimensional channels so narrow that they cannot pass each other may exhibit single file diffusion (SFD)*. Figure 4-1 visualizes this type of anomalous diffusion, where the sequential order of diffusing molecules is preserved. This results in a deviation from the usual time dependence of the mean square displacement (MSD) observed for normal diffusion. While MSD increases proportionally with time for normal diffusion, for SFD in sufficiently long channels when all boundary effects at the channel margins can be neglected, it grows with the square root of time

$$\langle z^2(t) \rangle = 2Ft^{1/2} \quad (4-1)$$

where F is the single-file mobility factor and t is the diffusion time.¹² Single-file systems exist in various fields, from living systems to catalysis.²²⁻²⁵ However, experimental evidence and understanding of diffusion in single-file systems is sparse. The work outlined in this chapter is aimed towards investigating the fundamentals of SFD of mixtures.

4.2 Review of Published Single-File Diffusion Studies

An important consequence of SFD is a significant slowdown in the growth of MSD with time in comparison to that for normal diffusion. This property opens a

* This chapter is based on previously published work. Reprinted with permission from: Dutta, A. R.; Sekar, P.; Dvoyashkin, M.; Bowers, C. R.; Ziegler, K. J.; Vasenkov, S., Relationship between Single-File Diffusion of mixed and pure gases in Dipeptide Nanochannels by High Field Diffusion NMR. *Chem. Commun.* **2015**, 51 (69), 13346-13349

Dutta, A. R.; Sekar, P.; Dvoyashkin, M.; Bowers, C. R.; Ziegler, K. J.; Vasenkov, S., Relationship between Single-File Diffusion of Gas Mixtures in Nanochannels of the Dipeptide α -Ala- α -Val: High-Field Diffusion NMR Study. *J. Phys. Chem. C.* **2016**, 120 (18), 9914-9919

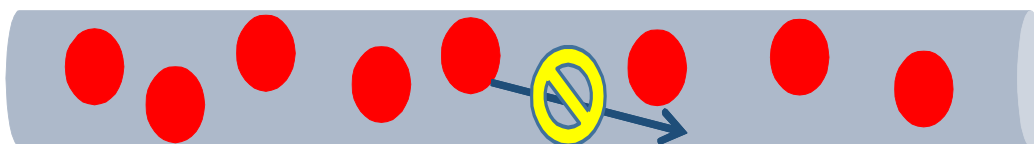


Figure 4-1. Schematic illustration of molecules restricted to move in a one-dimensional channel that has a radius smaller than the diameter of the molecules. Mutual passage is forbidden under these conditions.

possibility for highly selective separations if one component in the mixture exhibits normal diffusion and another SFD.^{12, 26-29} The potential use of this property in controlled catalysis has also been proposed.³⁰⁻³³ The integration of SFD in these applications has motivated studies of SFD in mixtures of different types of molecules using molecular-level simulations.

In particular, kinetic Monte Carlo simulations were performed to study counter-diffusion, tracer exchange and reaction under single-file conditions.³⁴⁻³⁵ Molecular simulations have also demonstrated that binary mixtures of small gas molecules diffusing in $\text{AlPO}_4\text{-5}$ molecular sieve can exhibit different diffusion regimes.²⁶ In one of these regimes both species in the mixture diffused according to the mechanism of SFD, and in another regime only one type of molecules exhibited SFD while the other exhibited normal diffusion. The potential application of this latter diffusion regime in molecular separations became the focus of Adhangale and Keffer, who investigated using molecular dynamics (MD) simulations, the diffusion of a methane/ethane mixture in $\text{AlPO}_4\text{-5}$.²⁷ A recently published analytical model based on the Maxwell–Stefan equations proposed using pure component mobilities and the corresponding adsorption isotherm data to estimate their mixture behavior in single-file systems.³⁶ More recently, an MD simulation study explored single-file mobilities as a function of loadings of binary gas mixtures in single-walled carbon nanotubes.³⁷

While diffusion of mixtures of different types of molecules in single-file channels has been the focus of many theoretical and simulations studies, there have been no previously published reports on experimental investigations of transport of sorbate mixtures under the SFD conditions. In section 4.5.1, the first experimental observation of SFD of molecular mixtures is presented. A thorough analysis of the relationship between the mobilities of pure sorbates and their corresponding mixtures is discussed in section 4.5.2.

4.3 Sorbent and Sorbates Studied

Self-assembled L-Ala-L-Val (AV) hydrophobic dipeptide crystalline nanotubes were used in these diffusion studies. AV is a microporous material containing helical channels of mean diameter (d) of $\sim 0.51\text{nm}$.³⁸ It was selected for this work because of recent studies of diffusion and tracer exchange of Xe atoms in AV nanochannels published by our group. These previous studies were performed using a combined application of ^{129}Xe PFG NMR and hyperpolarized ^{129}Xe spin tracer exchange NMR. These studies revealed that Xe in AV nanochannels is a highly ideal single-file system. AV nanotubes were purchased from Bachem and used as received. The average length of the AV crystal (L) is around 50 micrometers, as determined from the images recorded by a JEOL 6400 scanning electron microscope.³⁹

Diffusion of CO, CO₂, and CH₄ (Sigma-Aldrich, 99 atom% ^{13}C) in AV nanochannels was investigated by ^{13}C PFG NMR. These species were chosen because they simultaneously satisfy the spatial criteria for SFD observation and are industrially relevant gases. The spatial criteria require that the diameters of molecules are smaller than the diameter of AV channels, but greater than the radius of the channels. The latter requirement prevents mutual passage of the molecules. The kinetic diameters of CO,

CO₂, and CH₄ molecules are, respectively, around 0.34, 0.33, and 0.41 nm.⁴⁰ Clearly, all three species satisfy the SFD criteria for diffusion in AV nanochannels.

4.4 Experimental Details

PFG NMR can be used to directly measure the dependence of MSD on diffusion time in porous materials. Therefore, this technique is ideally suited for distinguishing SFD, characterized by the MSD scaling given by Eq 4-1.

Five millimeter diameter, medium-wall NMR tubes (Wilmad-Glass) were loaded with ~55 mg of AV nanochannels. Each tube was then, separately, connected to a custom-made vacuum system and the nanochannels were activated at an elevated temperature of 373 K overnight. The activation was performed under high vacuum conditions, at pressures below 0.001 mbar. This degassing of AV is intended to remove any initially present sorbates. The activation temperature is well below the AV melting point of 511 K.³⁸ Upon activation, each NMR sample was loaded with either a pure gas or a two-component gas mixture by cryogenic transfer of the corresponding gas or gas mixture from the calibrated volume of the vacuum system. The gas-loaded samples were flame sealed and separated from the vacuum system.

Three NMR samples loaded with one-component gas (CO, CO₂, and CH₄) and two samples loaded with two-component mixtures (CO/CH₄ and CO/CO₂) were prepared. The total gas pressure in the gas phase of each sample at 298 K was around 10 bar. In mixture samples, the partial pressure of each sorbate was 5 bar. For each sample the concentration of each gas in AV was determined by comparing the NMR signal of adsorbed gas(es) in these samples with the NMR signal in an NMR tube containing only pure gas at a known pressure, in the same way as discussed in previous work published by our group.⁴¹

Table 4-1. Gas concentration (in mol/kg of AV) obtained for the studied samples using NMR signal analysis.

	Single-Sorbate	CO/CH ₄	CO/CO ₂
CO	0.56 ± 0.06	0.34 ± 0.03	0.24 ± 0.02
CH ₄	0.48 ± 0.05	0.20 ± 0.02	-
CO ₂	0.52 ± 0.05	-	0.34 ± 0.03
Total gas concentration for mixture samples	-	0.54 ± 0.02	0.58 ± 0.03

The gas loadings for all samples are shown in Table 4-1. This table indicates that the total gas concentration in each sample was the same, within the limits of experimental uncertainty. It also shows that the concentration of each gas in the mixture was comparable. This is significant as it allows for direct comparison of the rate of the diffusion of the molecules in single-sorbate and mixture samples.

Longitudinal (T_1) ¹³C NMR relaxation times of the studied gases inside AV nanochannels were estimated using the 13-interval PFG NMR sequence by changing the time interval between the second and the third $\pi/2$ radiofrequency pulses of the sequence and keeping all other time intervals constant. Similarly, transverse (T_2) ¹³C NMR relaxation times were estimated using the same sequence by changing the time interval between the first and the second $\pi/2$ radiofrequency pulses of the sequence and keeping all other time intervals constant. Under the conditions of these measurements, it was confirmed that there was no attenuation of the signal due to diffusion of adsorbed gas molecules.

In all of the studied samples, the measured NMR relaxation data showed no evidence for distribution of T_1 and T_2 relaxation times for adsorbed gases. The T_1 NMR relaxation times for CO, CO₂, and CH₄ molecules adsorbed in the channels were estimated to be around 0.6, 2.7, and 1.5 s, respectively. The corresponding T_2 NMR

relaxation times for CO, CO₂, and CH₄ were found to be around 16, 18, and 22 ms, respectively. All diffusion and relaxation NMR measurements were performed at 298 K.

PFG NMR diffusion measurements were performed using a 17.6 T Bruker BioSpin NMR spectrometer operating at ¹³C resonance frequency of 188.6 MHz. The spectrometer is located at the National High Magnetic Field Laboratory's AMRIS facility in Gainesville, FL. Sine-shaped, bipolar magnetic field gradients with the effective duration of 1500-2200 μs were generated using a diff60 or diff30 diffusion probe (Bruker BioSpin) and Great60 gradient amplifier (Bruker BioSpin). The range of the gradient amplitudes used was between 0.3 and 23 T/m.

4.5 Observation of Single-File Diffusion in Mixtures

The 13-interval bipolar PFG NMR pulse sequence with longitudinal eddy current delay was used for all diffusion measurements. The longitudinal eddy current delay was between 3.5 and 5 ms. Diffusion data were obtained by measuring the PFG NMR signal intensity ($S(g)$) as a function of the magnetic field gradient (g) while keeping all other sequence parameters constant. For each type of the studied gas molecules S was equal to the area under the single ¹³C NMR line of these molecules. In the mixture samples, the different species were identified by their distinct ¹³C chemical shifts resulting in non-overlapping ¹³C NMR lines of these species. Under the measurement conditions, the ¹³C NMR chemical shifts CO, CO₂, and CH₄ were equal to 190.2, 135.6, and -5.4 ppm, respectively.

4.5.1 Attenuation Plots

Attenuation plots record the decrease in PFG NMR signal with increasing gradient strength, g , normalized to the signal obtained at the smallest gradient, as a

function of q^2 where q is equal to $2\gamma g\delta$, γ is the gyromagnetic ratio, and δ is the effective gradient duration. The attenuation (Ψ) is given by the following equation:

$$\Psi = \frac{S(g)}{S(g \approx 0)} \quad (4-2)$$

where $S(g)$ is the signal obtained with the application of gradient g and $S(g \approx 0)$ is the signal corresponding to the smallest gradient that can be accurately produced by the hardware. The PFG NMR echo attenuation due to one-dimensional diffusion in straight, randomly oriented, channels is expected to follow:

$$\Psi(q,t) = \frac{1}{2} \int_{-1}^{+1} \exp \left[-\frac{q^2 \langle z^2(t) \rangle r^2}{2} \right] dr \quad (4-3)$$

where $\langle z^2(t) \rangle$ is the MSD along the channel axis at diffusion time t . Equation 4-3 simplifies to the following expression after evaluation of the integral:^{12, 39, 42}

$$\Psi(q,t) = \sqrt{\frac{\pi}{2q^2 \langle z^2(t) \rangle}} \operatorname{erf} \left(\sqrt{\frac{q^2 \langle z^2(t) \rangle}{2}} \right) \quad (4-4)$$

It is important to note that due to the helical topology of the AV channels, the actual MSD inside the AV channels along the diffusion path ($\langle z^2 \rangle_{\text{helix}}$) is larger than the MSD along the channel direction ($\langle z^2 \rangle$) in Eq 4-4. The values of $\langle z^2 \rangle_{\text{helix}}$ can be estimated as $\langle z^2 \rangle p^2$, where p is the geometrical factor equal to 1.3. The value of this factor was determined using the values of the pitch of the helix (~ 1 nm) in AV channels and the maximum Xe atom capacity per unit pitch.⁴² Hence, for AV channels, Equation 4-4 can be re-written as:

$$\Psi(q,t) = \sqrt{\frac{p^2 \pi}{2q^2 \langle z^2 \rangle_{\text{helix}}}} \operatorname{erf} \left(\sqrt{\frac{q^2 \langle z^2 \rangle_{\text{helix}}}{2p^2}} \right) \quad (4-5)$$

For SFD in AV channels, Eq 4-1 can be substituted into Eq 4-5:

$$\Psi(q,t) = \sqrt{\frac{p^2\pi}{4q^2F_{\text{helix}}t^{1/2}}} \operatorname{erf}\left(\sqrt{\frac{q^2F_{\text{helix}}t^{1/2}}{p^2}}\right) \quad (4-6)$$

where F_{helix} denotes the single file mobility factor inside the AV channels, viz. mobility factor along the helical path. Figures 4-2 and 4-3 show examples of the measure ^{13}C PFG NMR attenuation curves as a function of q^2t . In the presentation of these figures, the attenuation curves measured for each sample and species at different times, but otherwise consistent conditions, are expected to collapse into a single curve if the MSD grows with the square root of diffusion time, as prescribed by Eq 4-1.

It is seen in Figures 4-2 and 4-3 that for each studied sample and type of molecules the attenuation curves measured for a broad range of diffusion times coincide, within experimental uncertainty, in this presentation of the figures. Hence, it can be concluded that in each case the diffusion process obeys the SFD mechanism. This is an expected result because the channel radius is smaller than the collision diameter of the studied molecules, leading to the SFD conditions for these molecules.

4.5.2 Mobilities of Sorbates in Pure and Mixture Samples

Figure 4-2 shows PFG NMR attenuation curves for the diffusion in AV channels loaded with a single gas. In Figure 4-2 (a), such curves are shown for CO and CH₄, i.e. the gases used in the CO/CH₄ mixture. In Figure 4-2 (b) the attenuation curves are shown for CO and CO₂, i.e. the gases used in the CO/CO₂ mixture. Attenuation curves measured for each single gas coincide within experimental error for the broad range of diffusion times reported. It is seen in Figure 4-2 that for each gas pair used in the mixtures the attenuation curves in the samples loaded with a single gas are different for

different gases. Least squares fit of the attenuation curves in Figure 4-2 for the samples loaded with the single gas (CO, CH₄ and CO₂) to Eq 4-6 resulted in the single-file mobility factors for these gases (Table 4-2). The corresponding best-fit curves are shown in Figure 4-2. Small deviations between the experimental data and the best-fit curves in Figure 4-2 for the single-component samples can result from some small differences between the actual distributions over the channel directions in the samples and the fully random distribution assumed in the derivation of Eq 4-6.

Figure 4-3 (a, b) shows PFG NMR attenuation curves for the diffusion of CO/CH₄ and CO/CO₂ mixtures in AV channels. It is seen in the figure that for each mixture the attenuation curves measured for different types of molecules in a mixture coincide within the experimental uncertainty. According to Eq 4-6, this coincidence of the attenuation data indicates that both types of molecules in a mixture diffuse with an identical single-file mobility factor F_{helix} . Identical transport rates for different types of molecules in a mixture are expected under the SFD conditions because under such conditions molecules cannot pass one another in the channels.

Hence, the observation of identical rates of transport for different types of molecules in the studied mixtures provides additional evidence for the SFD diffusion mechanism in the mixtures. Least-squares fit of all the attenuation curves measured for the same mixture type to Eq 4-6 resulted in the values of F_{helix} for the studied two mixtures that are reported in Table 4-2. The best-fit curves are shown in Figure 4-3. It is seen that there are some small systematic deviations between these curves and the measured data. In complete analogy with single-gas samples, these deviations can be attributed to some small differences between the distributions over the channel

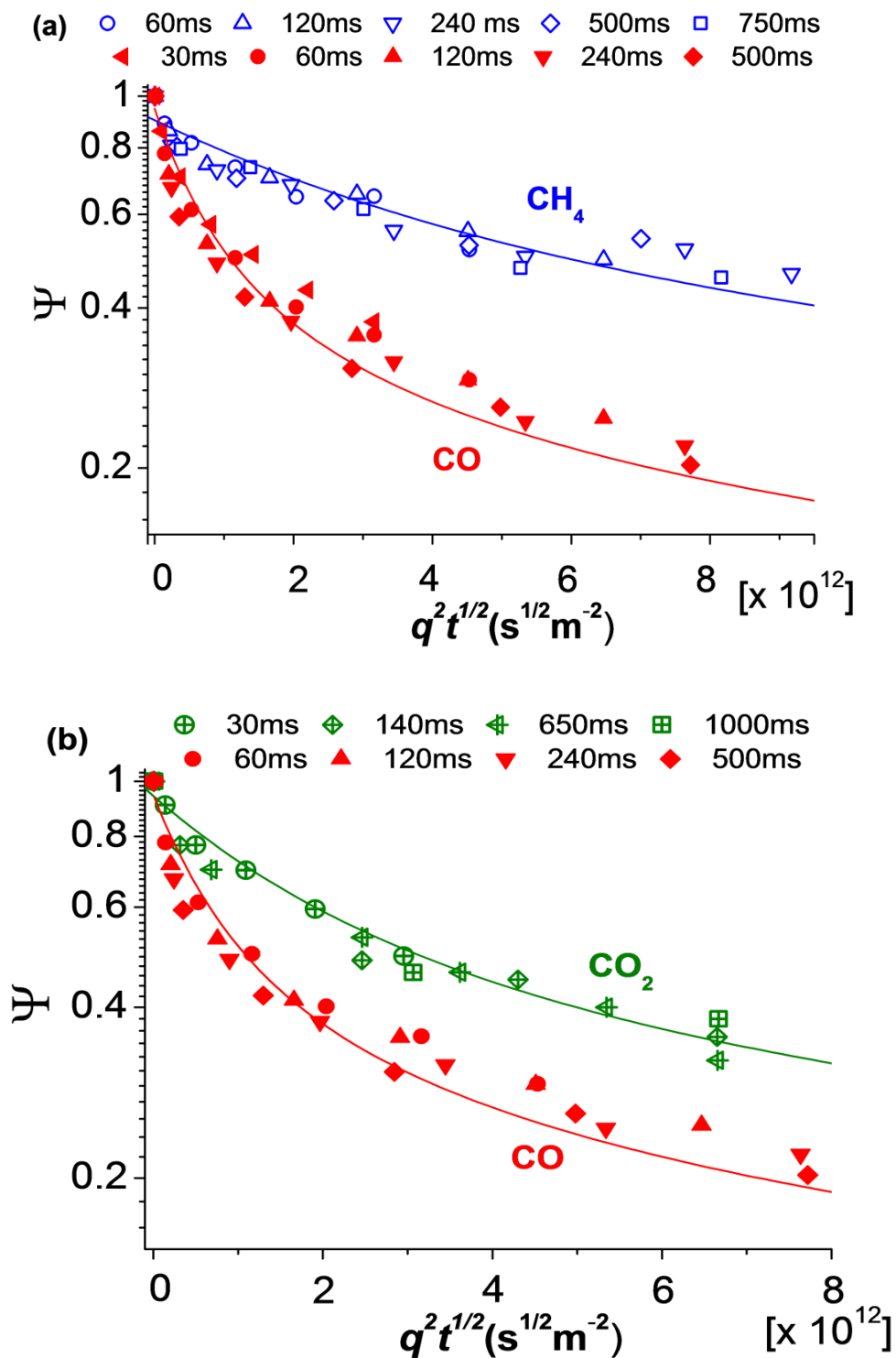


Figure 4-2. ^{13}C PFG NMR attenuation plots measured at 298 K for CO, CH_4 , and CO_2 diffusion in AV channels loaded with a single gas. The attenuation plots are shown for the following gases used to prepare the gas mixtures: (a) CO and CH_4 , and (b) CO and CO_2 .

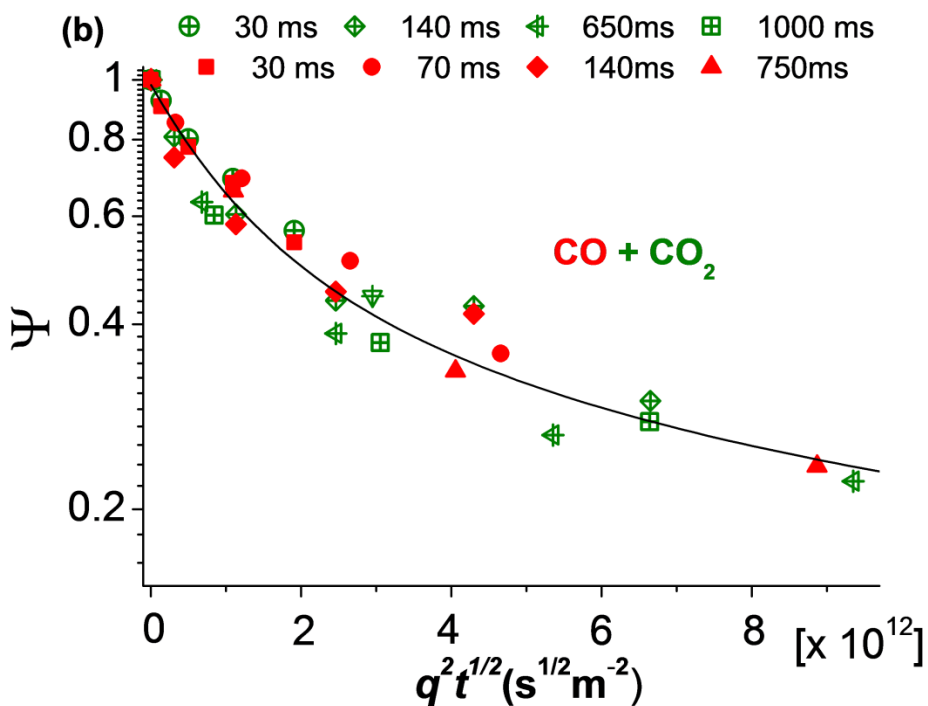
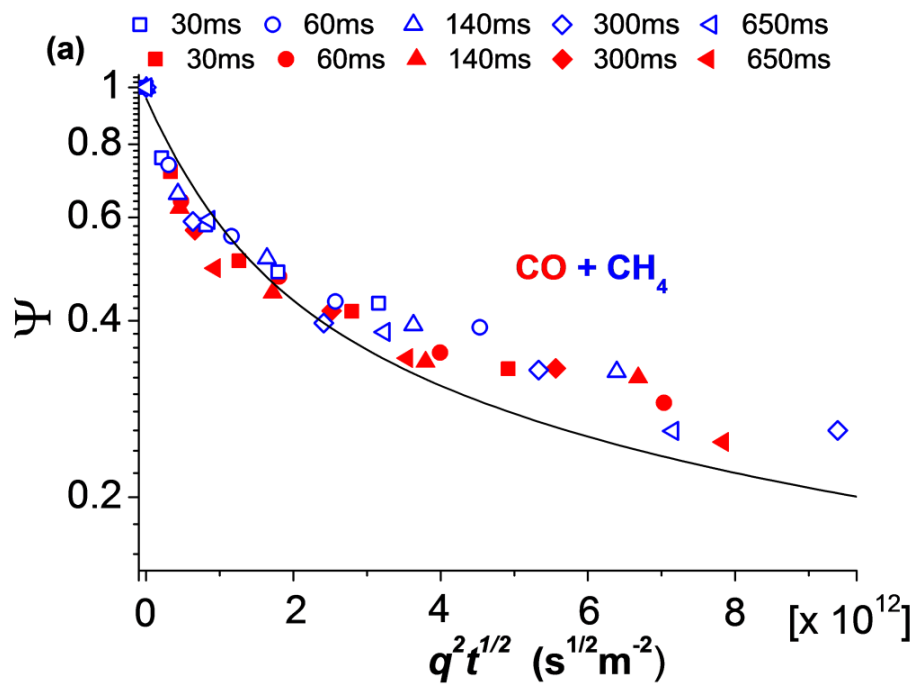


Figure 4-3. ^{13}C PFG NMR attenuation plots measured for CO, CH₄, and CO₂ diffusion in AV channels at 298 K. The attenuation plots are shown for the samples containing the following gas mixtures: (a) CO/CH₄, and (b) CO/CO₂.

Table 4-2. Single-File mobilities (F_{helix}) estimated from attenuation curves in Figure 4-1 and 4-2 using Eq 4-6.

	Mixtures		Single-Sorbate Samples		
	CO + CH ₄	CO + CO ₂	CO	CH ₄	CO ₂
$F_{\text{helix}} \times 10^{13}$ ($\text{m}^2 \text{s}^{-1/2}$)	31 ± 2	25 ± 2	46 ± 4	8.0 ± 0.6	15.0 ± 1

directions in the PFG NMR samples and a truly random distribution, which was assumed in the derivation of Eq 4-6.^{12, 39, 42}

Figure 4-4 presents the values of $\langle z^2 \rangle_{\text{helix}}$ as a function of diffusion time for each of the two mixture samples together with the corresponding data for the one-component samples. The MSD values were obtained from least-square fitting of individual PFG NMR attenuation curves measured for each sorbate and sample at each diffusion time to Eq 4-4. These values were then scaled to account for the helical topology as previously discussed. The proportionality between the values of MSD and square root of time in Figure 4-4 was verified by least square fitting of the data for each sample to Eq 4-1, where $\langle z^2 \rangle$ and F are substituted by $\langle z^2 \rangle_{\text{helix}}$ and F_{helix} , respectively.

In the double-logarithmic presentation of Figure 4-4, the best-fit lines are solid lines, which in all cases show a good agreement with the measured data. For comparison, the dashed line shows the linear growth of MSD with diffusion time which is expected for normal, Fickian diffusion. It was verified that the values of F_{helix} obtained from the fitting of the data in Figure 4-4 are in agreement, within experimental error, with the corresponding data in Table 4-2 which resulted from direct fitting of the attenuation curves.

Table 4-1 shows that the intrachannel gas concentration in each of the studied single-component samples was the same, within the experimental uncertainty. The

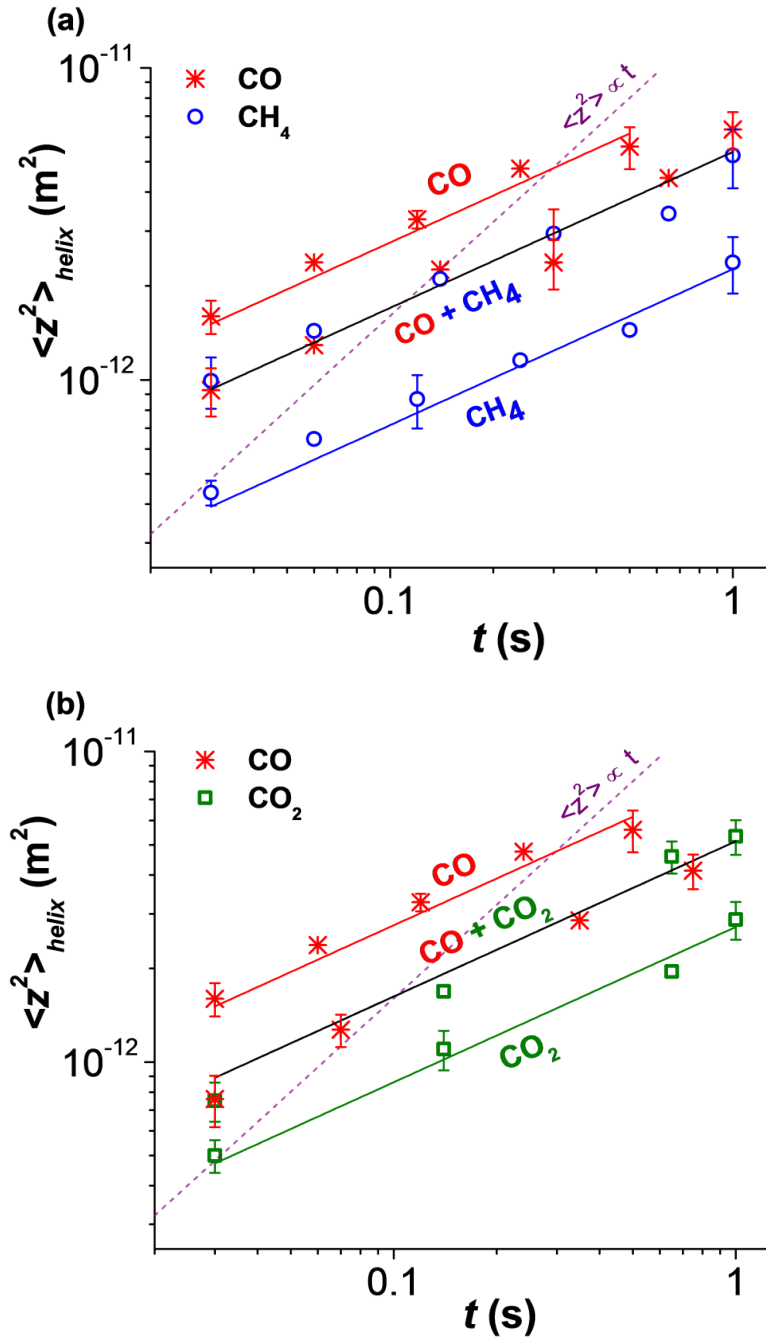


Figure 4-4. MSD dependence on times plotted on a double-log scale for (a) CO/CH₄ mixture and (b) CO/CO₂ mixture along with the corresponding single component samples. The MSD is obtained by fitting the attenuation curves shown in Figures 4-2 and 4-3 with Eq 4-4. The MSD reported here accounts for the helical topology of the channels. Solid lines are best-fit lines of the measured time dependences of MSD to Eq 4-1. Dashed line shows the growth of MSD with time expected for normal diffusion.

concentrations in the single-component samples were also nearly identical with the total gas concentration in the mixture samples, where the fractions of the individual gas components were comparable to each other (Table 4-1). All these considerations allow for a direct comparison of the single-file mobility factors in the single-component samples and their relationship with the single-file mobilities in the corresponding mixture samples.

The data in Table 4-2 indicates that in the single-component samples the fastest diffusing sorbate is CO, followed by CO₂ and CH₄. This trend in decreasing single-file mobilities of CO, CO₂ and CH₄ is consistent with the combination of larger molecular mass and size of CO₂ and CH₄ relative to CO. Table 4-2 shows that the single-file mobilities in the mixture samples is intermediate in comparison with the corresponding single-sorbate mobilities. This observation suggests that under the SFD conditions the replacement of the slower-diffusing molecules (CH₄ or CO₂) by an approximately the same number of faster-diffusing molecules (CO) in AV channels leads to a noticeable increase in the single-file mobility of the slower-diffusing sorbates.

In contrast, under the conditions of normal diffusion in microporous solids such a replacement of a fraction of a slower diffusing species by faster diffusing species often does not lead to any significant change in the diffusivity of the slower-diffusing molecules.¹² This difference between the SFD and normal diffusion of mixtures can be rationalized by noticing that under the conditions of SFD the displacement of any molecule strongly depends on the displacements of its next neighbors. Such dependence arises in SFD from the fact that movements of next neighbors determine the availability of space for displacements of any particular molecule.

In the studied mixture samples, fast local mobility of CO molecules surrounding CH₄ or CO₂ molecules can lead to faster diffusion of these CH₄ or CO₂ molecules in comparison to the single-component CH₄ or CO₂ samples. This consideration provides a tentative explanation for the difference between the single-file mobilities of CH₄ or CO₂ in the mixture samples in comparison to those in the corresponding single-component samples. However, further analysis and discussion presented in the next chapter indicate that the relationship between the single-file mobilities of the studied pure and mixed sorbates is likely related to molecular clustering.

4.6 Summary

Single-file diffusion of single-component gases and their binary mixtures in AV nanochannels was investigated by ¹³C PFG NMR at a high magnetic field using large field gradients for a broad range of diffusion times. The SFD mechanism was confirmed by verifying the proportionality of the MSD with the square-root of time for each sorbate in both single-component and mixture samples. This represents the first experimental evidence of SFD in a mixture of different types of molecules.

The SFD mobilities of both gases in the two-component mixture samples were found to be identical, which is consistent with the exclusion of mutual passages of molecules under the single-file conditions. At comparable total molecular concentrations in the channels, the mixture SFD mobilities were observed to be intermediate between their respective components' pure SFD mobilities. This relationship deviates from that observed for normal diffusion where the replacement of a fraction of a slower-diffusing component by a faster-diffusing one usually does not significantly influence the diffusivity of the former.

CHAPTER 5
ABSENCE OF TRANSITION TO CENTER-OF-MASS DIFFUSION

5.1 Single-File Diffusion in Finite Systems

Theoretical treatment and computer modeling of diffusion in channels of finite length under the SFD conditions predict a transition from the single-file regime to the center-of-mass (COM) regime at sufficiently large values of root MSD.^{14-15, 35} The COM diffusion is characterized by fully correlated displacements of all the molecules in any particular channel. Figure 5-5 illustrates the difference in molecular motion between SFD and COM diffusion.*

Consecutive movements of such molecular chains are not correlated with each other resulting in applicability of the laws of normal diffusion. In particular, a linear relationship between the MSD and diffusion time is expected in the COM regime. Hence, it is possible to define COM diffusivity in the same way as for normal diffusion by using the Einstein relation. COM diffusivity is greatly reduced in comparison to the diffusion coefficient under the conditions of normal diffusion, where an exchange of the relative positions of molecules in channels is allowed.

For the single-file diffusion process modeled as a random walk of particles with hard-core interactions, a transition from the SFD to COM regime is predicted to occur at the MSD given by the following relation:^{15, 35}

$$\langle z^2 \rangle_{\text{COM}} = \left(\frac{1-\theta}{\theta} \right) \frac{2l\lambda}{\pi} \quad (5-1)$$

* This chapter is based on previously published work. Reprinted with permission from: Dutta, A. R.; Sekar, P.; Dvoyashkin, M.; Bowers, C.R.; Ziegler, K.J.; Vasenkov, S., Possible Role of Molecular Clustering in Single-file Diffusion of mixed and pure gases in Dipeptide Nanochannels. *Microporous and Mesoporous Mater.* **2017**

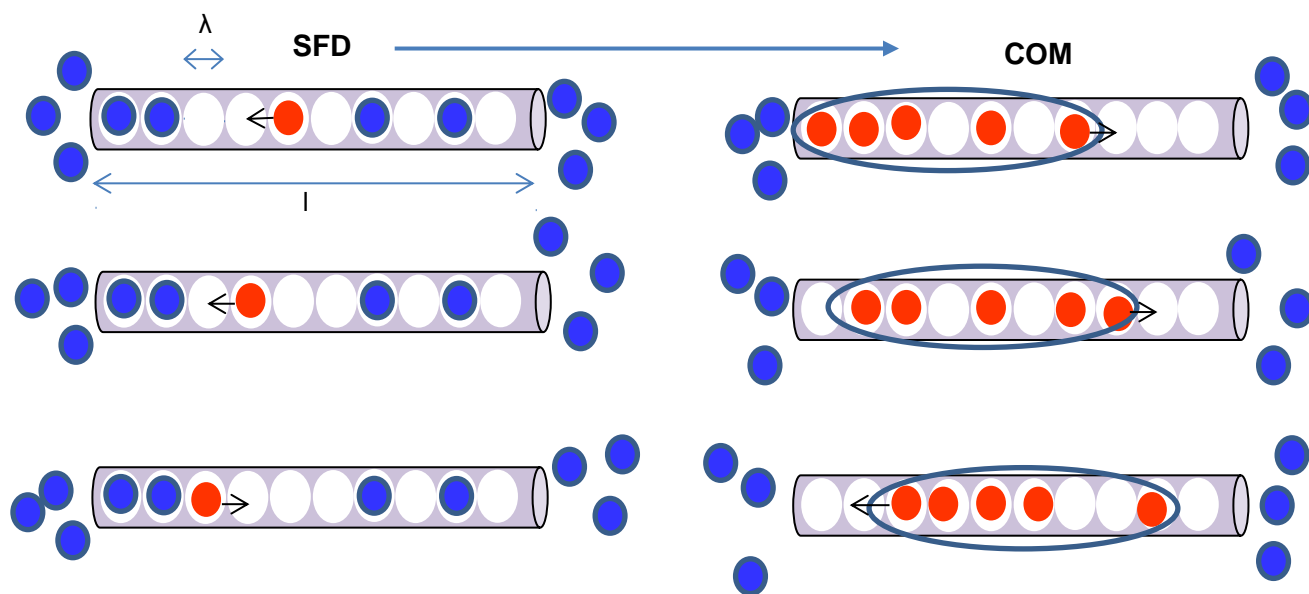


Figure 5-1. Illustration of difference in molecular motion in SFD and COM diffusion. After sufficient time in finite channels with fast exchange at boundaries, motion of molecules becomes extremely correlated and is independent of its previous movement, exhibiting Fickian motion.

where l is the channel length along the diffusion path, λ is the elementary displacement along this path, and θ is the fractional particle loading in the channels. However, such a transition is yet to be observed experimentally. For all mixture and one-component systems reported in Chapter 4, the crossover MSD was estimated using Eq 5-1. The parameters θ , l , and λ were estimated as described below.

The average channel length l along the diffusion path in Eq 5-1 was determined using the known average length of the studied AV crystals ($L = 50 \mu\text{m}$). This length corresponds to the channel length along the helix axis. The value of l was obtained by multiplying L with the geometrical factor $p = 1.3$, which was discussed earlier.

The fractional loading, θ , is the ratio of molecular concentration in the AV sample to the corresponding maximum theoretical concentration. Although the maximum theoretical concentrations for CO , CH_4 , and CO_2 in AV channels have not been

reported, these loadings can be estimated using the known maximum loading for Xe in these channels.³⁸ For each studied gas the maximum loading was roughly estimated as the maximum loading of Xe atoms in AV multiplied by the ratio of the kinetic diameters of Xe and the studied gas. Using the reported kinetic diameters, which are equal to 0.44, 0.34, 0.33, and 0.41 nm for Xe, CO, CO₂, and CH₄, respectively, the fractional loadings obtained for each sample are given in Table 5-1.^{40, 43}

The elementary displacement, λ , is traditionally defined in random walk based models as the distance between two adjacent sorbate molecules at a maximum loading in channels. Previous studies of Xe in AV channels have reported that the most efficient packing is achieved when Xe atoms are stacked abreast in a staggered arrangement.³⁸ The distance between two adjacent Xe atoms at the maximum loading was estimated to be $\frac{3}{4}$, of the kinetic diameter of a Xe atom. Owing to the similarity between the kinetic diameter of Xe atoms and gas molecules studied in this work the estimated λ for these molecules as $\frac{3}{4}$ of the kinetic diameter.

Table 5-1. Estimates of fractional loadings (θ), the values of MSD at which a transition from SFD to COM diffusion is predicted by Eq 5-1 ($\langle z^2 \rangle_{\text{COM}}$), and the minimum cluster size required by Eq 5-1 for not observing this transition under the reported experimental conditions of this study.

	Mixtures		Single-Sorbate Samples		
	CO + CH ₄	CO + CO ₂	CO	CH ₄	CO ₂
θ	0.22 ± 0.02	0.16 ± 0.02	0.20 ± 0.01	0.21 ± 0.01	0.18 ± 0.02
$\langle z^2 \rangle_{\text{COM}}$ (m ²)	5.6 × 10 ¹⁴	7.2 × 10 ¹⁴	5.4 × 10 ¹⁴	6.2 × 10 ¹⁴	5.9 × 10 ¹⁴
Minimum cluster size (number of molecules)	140	70	110	30	50

Table 5-1 lists the crossover MSDs, $\langle z^2 \rangle_{\text{COM}}$, obtained using Eq 5-1 with the parameters estimated as discussed above. It is seen that the values of $\langle z^2 \rangle_{\text{COM}}$ in Table

5-1 are in all cases smaller than the smallest MSD measured by PFG NMR (Figure 4-4). Hence, a linear dependence of MSD on time, a signature of COM diffusion, should have been observed for all samples under the reported experimental conditions. However, contrary to this, the experimental data in Figure 4-4 show the MSD dependence on diffusion time as given by Eq 4-1 for SFD.

5.2 Relationship between Single-File Mobilities

The theoretical model (Eq 5-1) and the experimental data presented in Chapter 4 can be reconciled if presence of long-range interactions between molecules is considered, which could induce molecular clustering. Formation of molecular clusters was previously demonstrated under the SFD conditions using MD simulations.⁴⁴⁻⁴⁶ These studies demonstrate that single-file diffusion of small gas molecules can be dominated by correlated movements of many molecules, viz. molecular clusters, rather than by movements of individual molecules.

In the scenario where individual molecules form large clusters that perform SFD, the actual elementary displacements, λ , in Eq 5-1 is determined by the size of clusters, which is much larger than the collision diameter of the molecules used to estimate the crossover values shown in Table 5-1. This change in λ shifts the transition MSD to larger values for all samples studied. Hence, by assuming that the minimum crossover MSD is as large as the greatest experimentally measured MSD, Equation 5-1 can be used to estimate the smallest cluster size for each system. This is done by using the inherent proportionality between the number of molecules in a cluster and λ and manipulating Eq 5-1 to evaluate λ corresponding to the largest MSD probed for a given system. The projected values of the minimum cluster sizes are reported in Table 5-1. They vary between 30 to 140 molecules, depending on the system.

The presence of molecular clustering in the context of single-file diffusion can also explain the relationship observed between the SFD mobilities of single-component sorbates and their mixtures. In accordance with the random walk model, the SFD mobility varies linearly with the product of λ and the square root of the diffusivity, \mathcal{D}_0 , of a single molecule/cluster in the infinite dilution limit.¹² \mathcal{D}_0 is expected to be inversely proportional to λ , which is determined by the cluster size. Hence, the SFD mobility value should be proportional to the square root of λ . Therefore, it can be expected that the single-component sorbate that exhibits the largest SFD mobility (CO) forms larger clusters than its slower counterparts (CH₄ and CO₂). One reason for CO molecules to form larger clusters than CH₄ and CO₂ can be related to dipole-dipole interactions between CO molecules. The average cluster in mixture samples would likely be intermediate in size with respect to their corresponding single-sorbate samples. This would translate into intermediate SFD mobilities of mixtures relative to their respective one-component sorbates, which is consistent with the experimental observations reported here. More studies are needed to investigate the clustering of molecules. In particular, measurements of adsorption isotherms can be useful. It is discussed in Ref 47 that the shape of the adsorption isotherm can reveal the extent of interaction between molecules, especially if it exceeds their interaction with the host.⁴⁷ Such a strong interaction could result in clustering. While such an analysis can be insightful in general, the framework of AV nanochannels is flexible and can alter with loading resulting in adsorption isotherms that become difficult to interpret conclusively.

In addition to molecular clustering discussed above, the existence of strong transport barriers at the ends of AV channels can be responsible for the absence of a

transition to COM diffusion at the MSDs reported in Table 5-1.^{15, 35} Such transport barriers, however, are not expected to appreciably extend the length scale of the SFD regime, which remains unperturbed by boundary effects at the channel ends. Since the MSD time scaling of SFD (Eq 4-1) is observed for all sorbates, both in pure and mixture form, at length scales beyond those of COM transition, it is unlikely that transport barriers are singularly responsible for preventing this transition. However, additional theoretical studies are needed to clarify the contribution of transport barriers at channel boundaries to the transition from SFD to COM diffusion.

The existence of clusters can be experimentally investigated through techniques such as Fourier Transform Infrared Spectroscopy. The exact size of these clusters, however, would be difficult to corroborate given the resolution limitations of FTIR. Distinguishing between clusters consisting of molecules in the wide range between 50 to 150 molecules is challenging under the conditions of this experimental technique. A possible combination of experimental and computational study is recommended to provide further insight into the role of clusters in this study.

5.3 Summary

Simulation studies and theoretical considerations predict a transition from the SFD to COM regime at sufficiently large diffusion times. The crossover is characterized by a shift from the MSD dependence on the square root of time to a linear dependence on time. However, this transition to COM regime was not experimentally observed for any of the systems studied. Molecular clustering is proposed to explain the absence of this transition. Equation 5-1 was used to estimate the minimum cluster size needed to sustain SFD under our experimental conditions. The clustering hypothesis was also used to qualitatively explain the unique relationship between the SFD mobilities of

components in the single-sorbate and mixture samples. This data suggests that molecular clustering in single file channels can be one of the main factors determining the rate of single-file diffusion of mixed and pure sorbates.

CHAPTER 6 METHODOLOGY DEVELOPMENT- CALIBRATION OF MAGIC ANGLE SPINNING PROBE FOR NMR DIFFUSOMETRY

6.1 Motivation

Pulsed Field Gradient NMR is a powerful technique to investigate diffusion in porous materials. Our group, in conjunction with the National High Magnetic Field Laboratory, has developed an experimental setup that combines high magnetic field and large field gradients to study diffusion properties on different length scales in nanoporous and microporous materials. However, there are some difficulties associated with such materials, especially when studying mixture sorbates.⁴⁸ Firstly, the restricted mobility of molecules in pores can result in line broadening. Secondly, differences in local magnetic fields originating from sample heterogeneities can contribute further to large broadening of the signal. This effect of line broadening limits the applicability of PFG NMR and the corresponding reduction in resolution can inhibit identification of components in mixtures, principally for ^1H NMR. Thirdly, the line broadening also manifests the reduction in T_2 NMR relaxation times, which restrict the duration of gradients that can be applied and hence restricts the range of displacements that can be probed.

The combination of Magic Angle Spinning (MAS) with PFG NMR presents a possible solution to the listed challenges associated with conventional PFG NMR.⁴⁹⁻⁵⁰ In the MAS setup, the sample is oriented at an angle of 54.7° with respect to the magnetic field, as portrayed in Figure 6-1, and rotated about this axis at a desired frequency.¹⁷ Influence of anisotropic interactions such as dipolar coupling and susceptibility effects on the line width and related T_2 NMR relaxation time can be reduced or suppressed

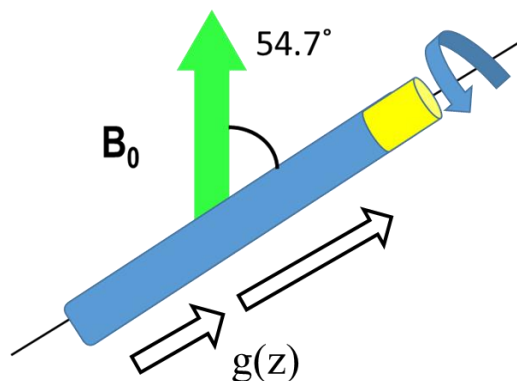


Figure 6-1. A schematic of the MAS experimental setup combined with the pulsed field gradient coil, $g(z)$, in a high-resolution MAS probe. The spinning axis along which the sample is oriented is at an angle of 54.7° with respect to the external magnetic field, B_0 .

completely by adopting the MAS experimental design. The extent of suppression depends on the interaction strength and the achievable rotation frequency.

The combination of MAS and PFG NMR to study diffusion of single and multi-component sorbates in various host materials, including zeolites has been successfully demonstrated by others.^{49, 51-53} To enhance the capability of PFG NMR at the National High Magnetic Field Laboratory (NHMFL), this methodology of MAS PFG NMR calibration and testing was introduced at its facility at UF. This chapter is devoted to the development of this experimental setup on the 600 MHz Bruker NMR spectrometer located at the AMRIS facility of the NHMFL.

6.2 Gradient Calibration

The high-resolution MAS probe available at the NHMFL at UF supports a 4 mm rotor and is equipped with gradient coils. The steps involved in making this probe usable for PFG NMR measurements are outlined as follows:

- determine strength of gradient
- evaluate gradient uniformity
- perform temperature calibrations
- test accuracy of technique using diffusion measurements

The absolute value of the gradient strength was determined by recording the image (^1H NMR) of a spacer of known precise thickness, immersed in a solution of $\text{H}_2\text{O}/\text{D}_2\text{O}$, in the presence of an applied field gradient. From the resulting spectra, the maximum gradient strength, g_l , of the coil can be calculated by:⁵⁴

$$g_l = \frac{\Delta\omega}{\epsilon\gamma g_a} \quad (6-1)$$

where $\Delta\omega$ is the width of the image of a spacer of known length, ϵ , obtained at a controlled gradient strength, which is indicated by a dimensionless parameter, g_a , expressed as the percentage of the maximum possible gradient strength, and γ is the gyromagnetic constant of protons. Two spacers of different lengths, 2.9 mm and 4.0 mm, were used for measuring g_l . The images of each of these spacers were recorded for different values of g_a , to improve both the accuracy and precision of the measurement. For these experiments the samples were oriented along the magic angle axis but remained static.

Table 6-1 shows the calculated values of the maximum gradient strength estimated using both spacers and the method described above. Based on this data, the gradient strength of the high-resolution MAS probe is determined to be 0.56 ± 0.01 T/m. It should be noted that the value of g_l measured using the longer spacer of 4 mm can generate a larger error associated to it. This is because there is expected to be greater variation in the magnetic field and the gradient strength at the edges of the rotor as compared to its middle. Hence, the longer sample is susceptible to these deviations, resulting in decreased confidence in the calculated value of g_l .

Evaluating the uniformity of the gradient along the rotor axis is essential to assessing the potential accuracy of PFG NMR measurements. Large variations in the

Table 6-1. Values of maximum gradient strength, g_l (T/m), calculated using Eq 6-1 for two spacers of varying lengths.

g_a	$\epsilon=2.9$ mm	$\epsilon=4.0$ mm
10 %	0.55	0.51
20 %	0.57	0.57
30 %	0.57	

gradient profile along the length of the rotor can translate to inaccurate measurements of diffusivities. To assess the uniformity, a pulse sequence proposed by Hurd et al was employed.⁵⁵ It is composed of a Hahn echo with two gradient pulses, g , before and after the 180° refocusing pulse and in which the echo is acquired during the application of another gradient (g_r). Spectrum acquisition under the conditions of a large gradient, g , results in a heavily diffusion weighted profile. Comparison of such spectra with application of a weak and strong gradient can provide insight into the uniformity of the gradient strength along a chosen axis.

This sequence was used on a sample of H_2O that filled the length of the rotor. Under static conditions, the spectrum of the sample was obtained at two different gradient strengths, 6% and 50%. Figure 6-2 shows the gradient profile obtained at the mentioned gradient strengths. By normalizing the intensity of the NMR signal obtained at smallest gradient strength (0.03 T/m) to the largest gradient strength (0.28 T/m) applied, the variation in the gradient profile along the magic angle axis is captured. This normalized intensity along the length of the rotor is shown in Figure 6-3. While there is large variation along the edges of the rotor caused by experimental artefacts, the gradient profile is essentially flat along the bulk of the rotor axis.⁵⁴ Hence, there is sufficient uniformity of the gradient to proceed with further calibration.

Accurate diffusion measurements require precise control and knowledge of the sample temperature. Under MAS conditions, where the sample is rotating at rates as large as 8 kHz, there is a potential for the temperature of the sample to vary with the application of this mechanical force. While this change in temperature is also a function of the thermal conductivity of the sample itself, this contribution cannot be generalized. However, an assessment of temperature variation as a function of spinning rate can be performed as a preliminary correction for accurate sample temperature control.

The actual sample temperature was systematically estimated using neat methanol under various spinning conditions. Neat methanol can be utilized as an NMR thermometer as the difference in frequency of its two proton peaks is a strong function of temperature it experiences.⁵⁶ This dependence on temperature has been well established in literature and the corresponding empirical formula was used here to estimate the temperature of the sample (neat methanol) at different spinning rates and system temperatures. The system temperature corresponds to the temperature that is set by the user for the NMR spectrometer to operate at.

Figure 6-4 plots the sample temperature of methanol as a function of the system temperature for spinning rates in the range of 4 kHz to 8.5 kHz. As anticipated, the increase in sample temperature from the system temperature is larger for higher spinning rates. The deviation of the sample temperature can be as large as 8 K. The data presented in Figure 6-4 is fit with the least-squares line that predicts sample temperature (y) as a function of system temperature (x). These formulas can be used to determine the system temperature that should be used for a desired sample temperature at a given spin rate during diffusion measurements.

The final assessment of the accuracy of gradient and temperature calibration in this MAS PFG NMR setup culminates in the measurement of self-diffusivity of water. Figure 6-5 compares the attenuation plots obtained using the 13-interval sequence under various conditions of a sample of water in a 4 mm rotor. There is very strong agreement between the attenuation curves acquired under static conditions and two different spinning conditions (4 kHz and 5 kHz).

The system temperatures were set based on the temperature calibration presented in Figure 6-4 such that the sample temperature corresponded to 298 K. In addition, two different diffusion times (50 ms and 200 ms) were observed for each spinning rate to evaluate the gradient calibration. Given the consistency in the attenuation curves for all these conditions, a single least-square fit was obtained as shown in Figure 6-5. The corresponding self-diffusivity of H₂O at 298 K as evaluated from this fit is $(2.2 \pm 0.1) \times 10^{-9} \text{ m}^2/\text{s}$. This value is consistent with the published value of self-diffusivity of water at 298 K, obtained using conventional PFG NMR.

6.3 Reference Measurement in Microporous Material

After establishing this new methodology through the preliminary measurements of free water, a progression was made towards performing measurements on porous materials. As discussed in the beginning of this chapter, there are limitations to PFG NMR related to studying diffusion in nanoporous and microporous materials. Hence, the MAS PFG NMR setup was used to demonstrate its potential in investigating diffusion in porous structures, specifically zeolitic imidazolate framework (ZIF). ZIF-8 is a MOF that consists of zinc ions coordinated with four imidazolate rings. ZIF-8 was saturated with H₂O and the self-diffusivity of adsorbed H₂O was measured by employing MAS PFG NMR.

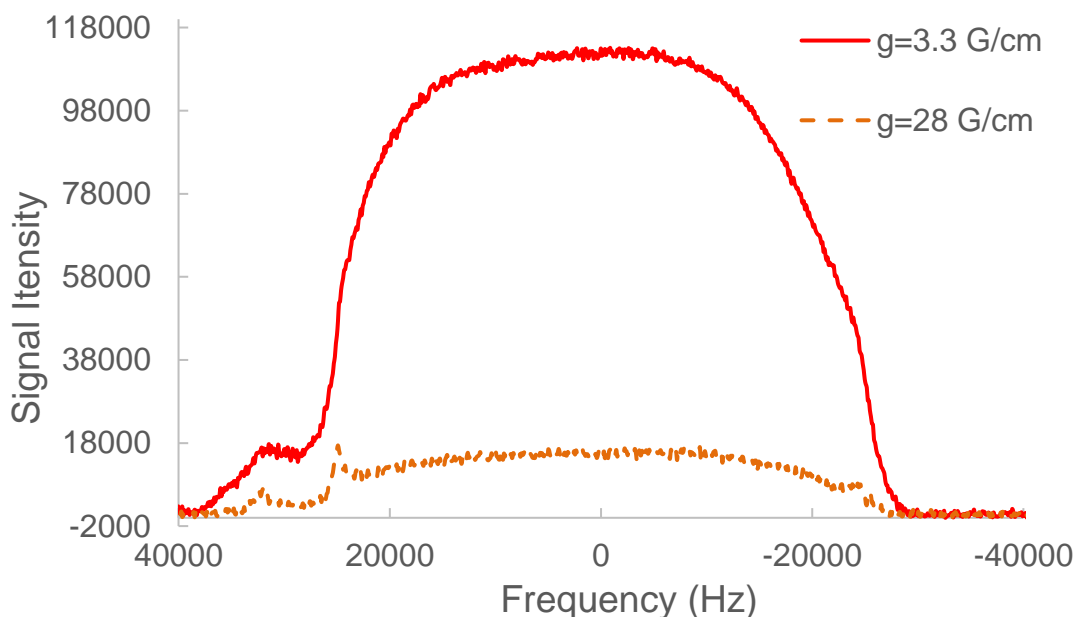


Figure 6-2. The image profile acquired along the rotor axis for a mixture of H₂O/ D₂O at two gradient strengths. The sample was oriented along the 57.4° but kept static.

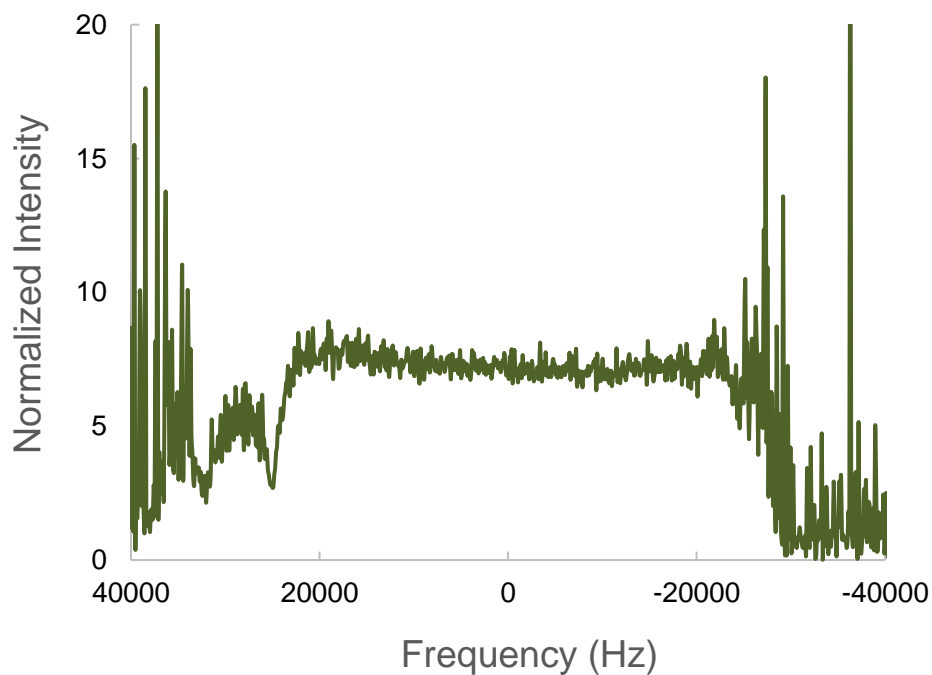


Figure 6-3. A plot of the NMR signal obtained at the smallest gradient strength normalized to the signal recorded at the largest gradient strength. The presented gradient profile shows that the gradient is uniform along most of the magic angle rotor axis.

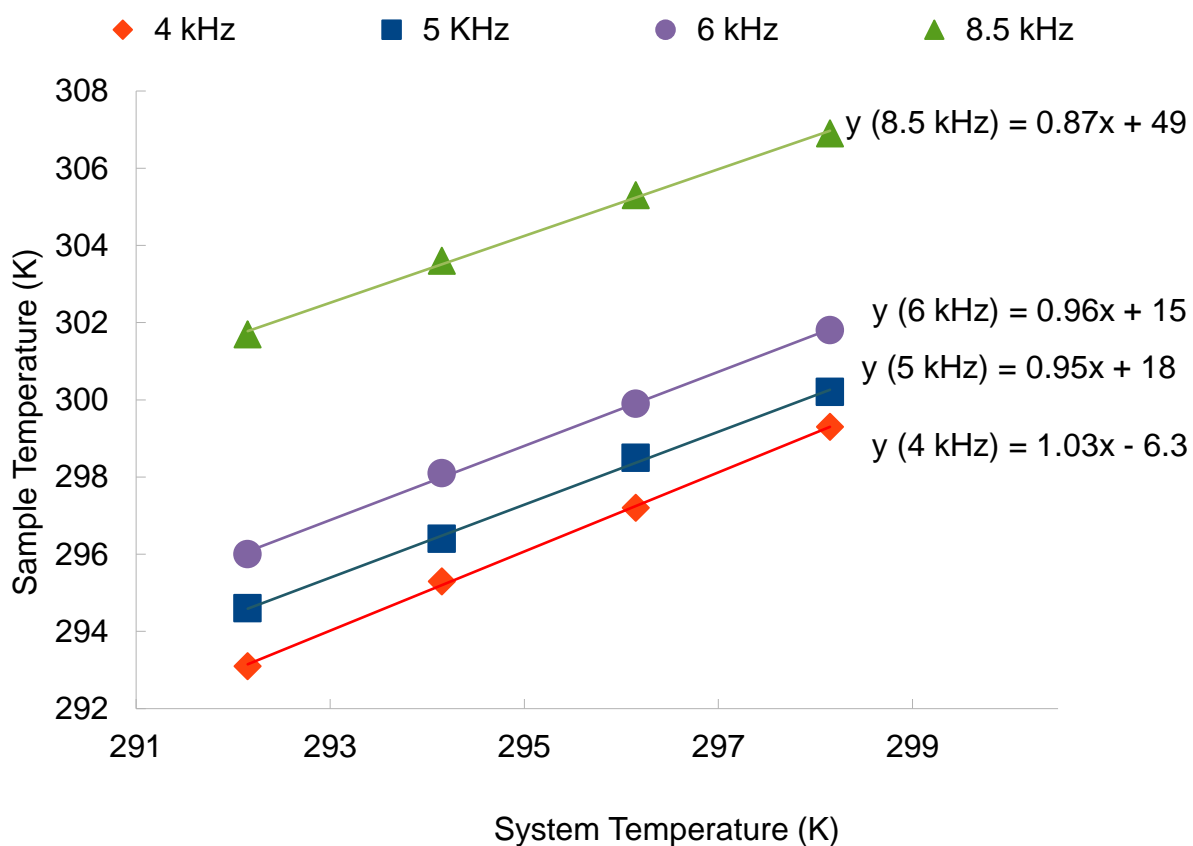


Figure 6-4. The temperature dependence of sample temperature on the spin rate plotted as a function of the system temperature determined using neat methanol. The formulas listed are obtained by the least-squares fit and relate the system temperature (x) to the sample temperature for spin rates between 4 kHz and 8.5 kHz.

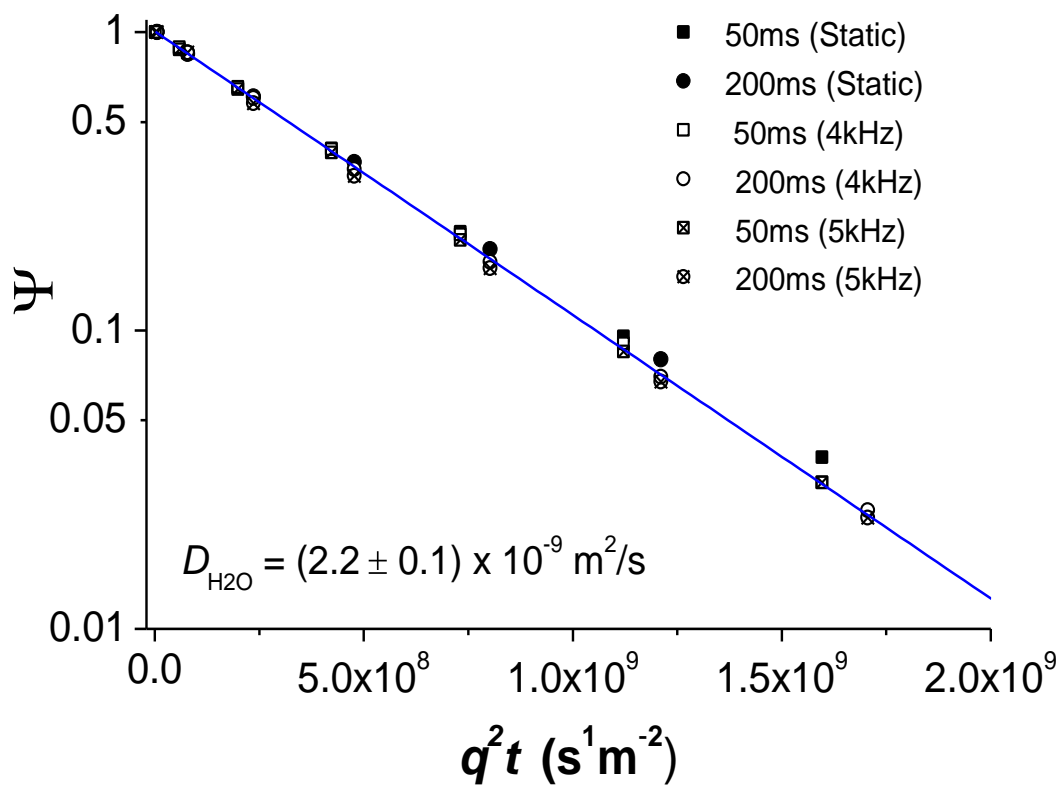


Figure 6-5. Attenuation plots acquired using the MAS PFG NMR setup at various spin rates and diffusion times for a sample of water at 298 K. Due to the strong agreement between the various attenuation curves a single least-squares line was fit to describe them.

Before saturating ZIF-8 with water, a conventional ^1H NMR of ZIF-8 (non-activated) was acquired under conditions of MAS at a spin rate of 7 kHz. Figure 6-6 illustrates how effective MAS can be at improving spectral resolution. The two large peaks with line widths between 900 Hz and 1200 Hz belong to the protons in the ZIF-8 framework. The peaks marked with an asterisk are spinning side bands. The much narrower peak with a width of 40 Hz is assigned to the water present in ZIF-8. This material was not activated and hence was expected to contain some water adsorbed under ambient conditions. For comparison, the line width of adsorbed water measured using this spectrometer with a conventional PFG NMR probe is around 1200 Hz. Figure 6-7 compares the spectrum obtained of H_2O in a saturated bed of ZIF-8 as obtained under MAS conditions and static conditions. A vast improvement in the line-widths is observed under MAS conditions.

The ZIF-8 bed was then saturated with water and after equilibration was introduced into the calibrated high-resolution MAS probe. Figure 6-8 shows the overlay of ^1H spectra at different gradient strengths obtained using the 13-interval PFG NMR sequence with eddy current delays at a spin rate of 5 kHz. For the spectra shown, a diffusion time of 200 ms was allowed and sine-shaped gradient pulses of duration 2 ms were applied. Diffusion times in the range of 40 ms to 200 ms were investigated to provide a comprehensive understanding of self-diffusivity of water in ZIF-8.

The two overlapping peaks observed in Figure 6-8 can be assigned to water molecules in two different environments i.e., confined and unconfined (free) water. The slower attenuating, narrower peak might belong to the molecules inside the pores of the ZIF while the faster diffusing, slightly broader peak might be assigned to free water that

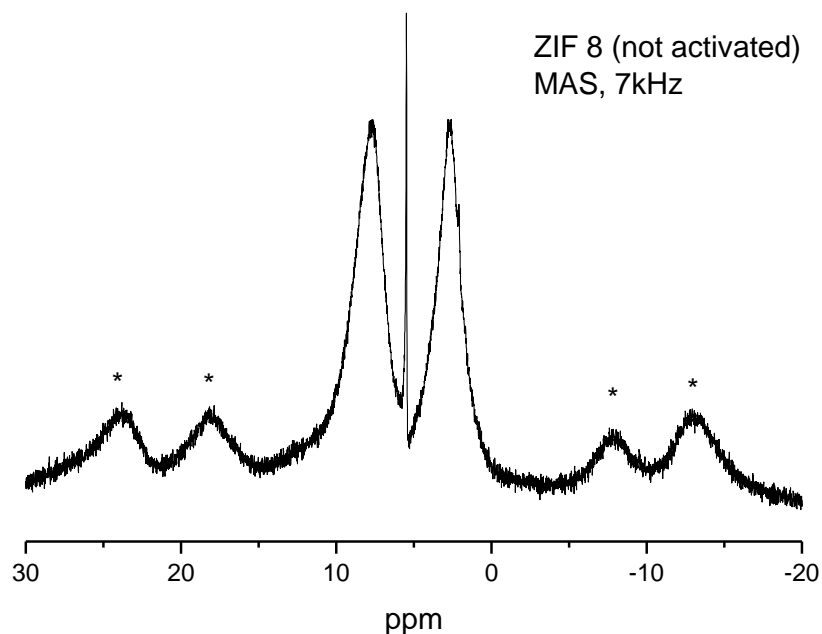


Figure 6-6. The ^1H NMR spectrum of non-activated ZIF-8 bed obtained using the high-resolution MAS probe. The sample was rotated at 7 kHz. The asterisk mark the spinning side bands and the remainder of the peaks are assigned to the protons of the ZIF-8 framework and residual, adsorbed H_2O .

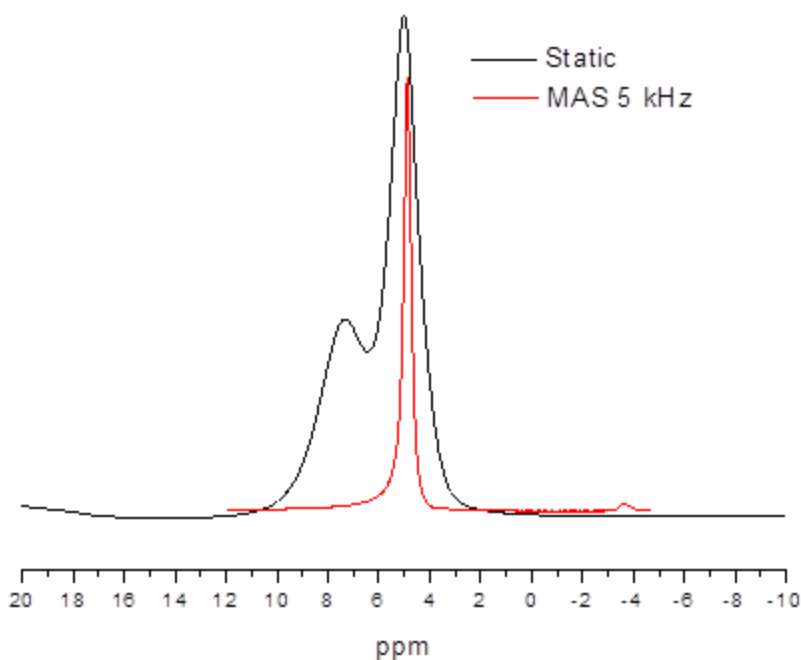


Figure 6-7. ^1H spectrum obtained of H_2O molecules in a saturated ZIF-8 bed under conditions of MAS and static NMR. There is a vast improvement in line-widths under MAS conditions

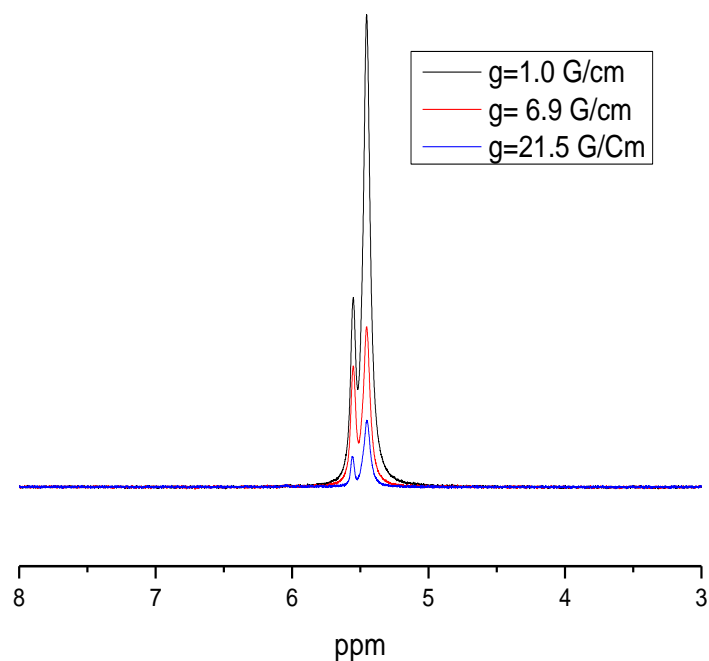


Figure 6-8. Overlay of the attenuating signal of H₂O saturated in the ZIF-8 bed resulting from increasing applied gradient. The two overlapping peaks belong to two water molecules in different environments of the ZIF-8 bed.

is either between the crystals of the material or in a thin layer that coats the surface of the crystals. The peaks from the framework essentially disappear in these experiments due to their significantly shorter T_2 relaxation times in comparison to that of water.

Under standard, static NMR conditions, overlapping peaks are difficult to resolve into individual ones due to large deviations from Lorentzian line shapes. However, under the stated MAS conditions, each overlapping peak can be deconvoluted using software. As a thorough analysis, two different approaches are demonstrated here to evaluate the diffusion properties of H₂O in ZIF-8.

In the first approach, the two peaks were treated as one and the attenuation of the signal was calculated by normalizing the integrated area of the combined peaks. Figure 6-9 shows the resulting attenuation curves corresponding to each reported diffusion time. It is clear from this figure that a bi-exponential curve is required to

characterize the two different diffusivities that pertain to each peak. The following equation was used to fit each attenuation curve individually:

$$\Psi = \frac{S}{S_0} = \sum_{i=1}^2 p_i \exp[-q^2 t \mathcal{D}_i] \quad (6-2)$$

where p_i corresponds to the fraction of molecules exhibiting diffusivity \mathcal{D}_i .

Table 6-2 lists the fitted values for each diffusion time obtained using Eq 6-1. The diffusivity of the slower ensemble of molecules is approximately $(1.1 \pm 0.3) \times 10^{-10} \text{ m}^2/\text{s}$ and is consistent with the diffusivity of adsorbed water molecules in ZIF-8, $\sim 1 \times 10^{-10} \text{ m}^2/\text{s}$, measured using conventional PFG NMR.

For consistency, the comparison of fitted values for the attenuation curves acquired under the same gradient duration is appropriate. From Table 6-2, the diffusivity of the faster ensemble of molecules is $(4.4 \pm 0.4) \times 10^{-9} \text{ m}^2/\text{s}$. The faster diffusivity, which is notably larger than that of bulk water, can be tentatively assigned to molecules exchanging between ZIF crystals and the volume between the crystals occupied by water in the liquid and/or vapor phase during the diffusion time used. Also, the trend of increasing fraction with diffusion time for the faster ensemble of molecules is a signature of long-range diffusion, i.e. diffusion under conditions of fast exchange between intra-ZIF volume and the liquid or vapor phase between ZIF-crystals.

Table 6-2. Ensemble fractions and the corresponding diffusivities obtained by fitting Eq 6-1 to the bi-exponential attenuation curves in Figure 6-8.

Diffusion Time (ms)	Gradient Duration (ms)	p_1	$\mathcal{D}_1 \times 10^9 \text{ (m}^2/\text{s)}$	p_2	$\mathcal{D}_2 \times 10^{10} \text{ (m}^2/\text{s)}$
100	2.0	0.74	4.5 ± 0.4	0.26	1.2 ± 0.2
150	2.0	0.78	4.4 ± 0.4	0.22	0.96 ± 0.2
200	2.0	0.82	4.6 ± 0.4	0.18	1.1 ± 0.3

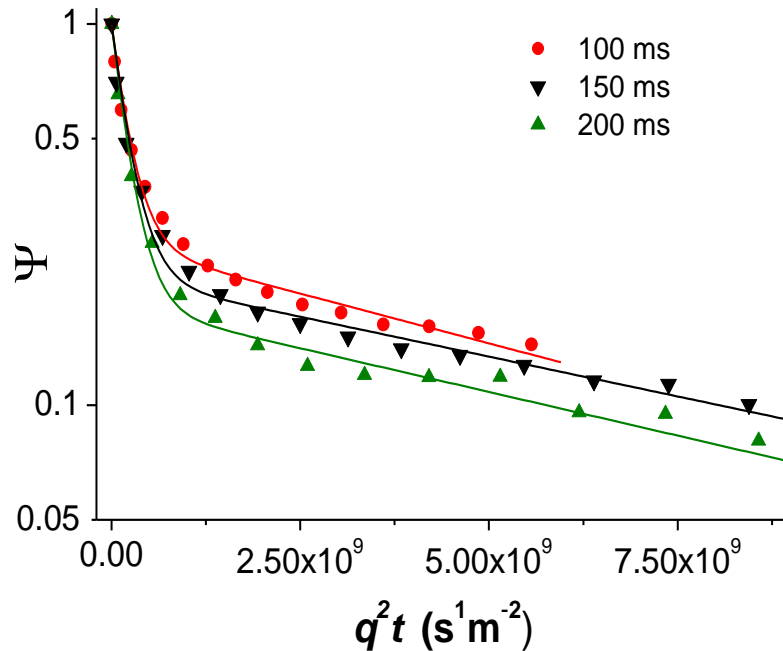


Figure 6-9. Measured PFG NMR attenuation curves for H₂O diffusion in a saturated ZIF-8 bed under MAS conditions with a spin rate of 5 kHz. The measurements were performed using the 13-interval sequence with eddy current delay. All measurements were performed at a sample temperature of 298 K.

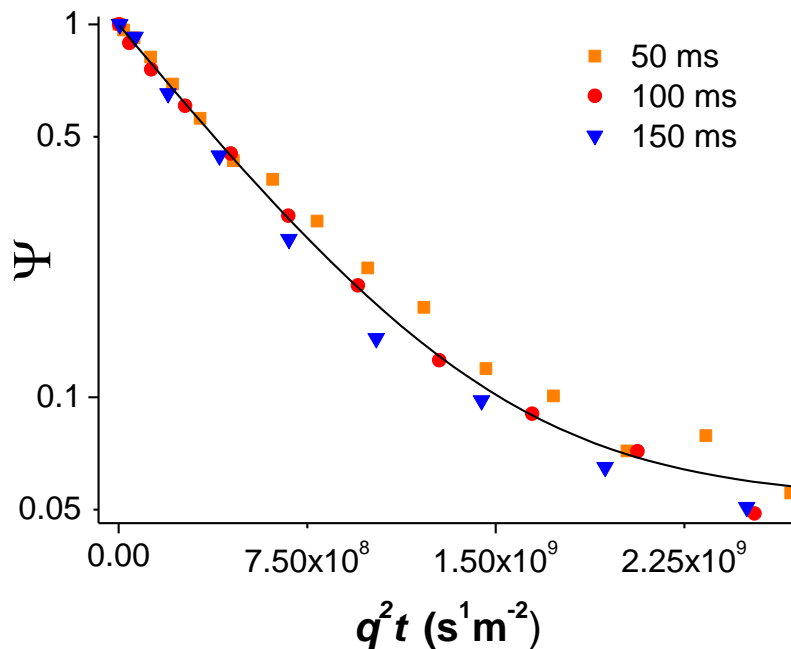


Figure 6-10. Attenuation curve obtained using deconvolution of overlapping peaks observed in the PFG NMR spectra of H₂O diffusion in ZIF-8. These attenuation curves correspond to the narrower, slower diffusing peak.

In the second approach, software was used to deconvolute the overlapping peaks into two distinct Lorentzian peaks and the corresponding attenuation curves obtained at different diffusion times are shown in Figure 6-10. To keep the comparison brief, the attenuation curves for just one of the peaks is discussed here. The attenuation curves in Figure 6-10 correspond to the narrower, slower diffusing peak as it is assigned to the adsorbed molecules in ZIF-8 pores. Since there is an exchange of water molecules inside the pores and the environment outside, there is some deviation from the mono-exponential behavior expected after deconvolution. Hence, a bi-exponential fit is used to describe all attenuation curves in Figure 6-10. The diffusivity of 0.93 fraction of molecules is estimated to be $(1.2 \pm 0.3) \times 10^{-10} \text{ m}^2/\text{s}$ and agrees very closely with the diffusivity of adsorbed water molecules as measured by the first approach. The corroboration of the diffusivities as calculated by the two approaches provides further confidence in the interpretation of the results reported.

6.4 Summary

Combining magic-angle spinning with pulsed field gradient NMR expands the range of porous systems that can be explored due to the remarkable gains in resolution. To exploit these advantages, a MAS probe was calibrated for diffusion measurements in collaboration with the National High Magnetic Field Laboratory. The gradients of a high-resolution MAS probe were calibrated and tested to perform diffusion measurements. This experimental setup was also used to demonstrate the accuracy of PFG NMR measurements in porous materials under MAS conditions.

While MAS PFG NMR offers a promising alternative to conventional, static PFG NMR, it is limited by the maximum strength of the gradient. The state-of-the-art gradient probes available can produce gradients as large as 30 T/m. Whereas, most high

resolution MAS probes are equipped to apply gradients up to 0.50-0.60 T/m. Depending on the sorbate and host molecules of interest, a suitable experimental setup should be chosen.

CHAPTER 7
WORK IN PROGRESS: DIFFUSION IN THE PRESENCE OF HYDROGEN SULFIDE

7.1 Motivation

Zeolitic Imidazolate Frameworks (ZIFs) are composed of imidazolate linkers and metal ions and are a subclass of metal organic frameworks (MOFs). Recently, there has been an explosion in research studies devoted towards synthesizing ZIFs and integrating them in industrial applications.⁵⁷⁻⁵⁸ This is because ZIFs possess properties such as large surface area, exceptional chemical and thermal stability, and high crystallinity which make them attractive candidates for membrane-based separations applications.⁵⁹⁻⁶² Their vast functionality and tunable pore size can be exploited to tackle challenging gas separations. The Energy Frontiers Research Center (EFRC) in Atlanta is devoted to studying these materials for acid gas separations and the results presented here are in an effort to further this goal.

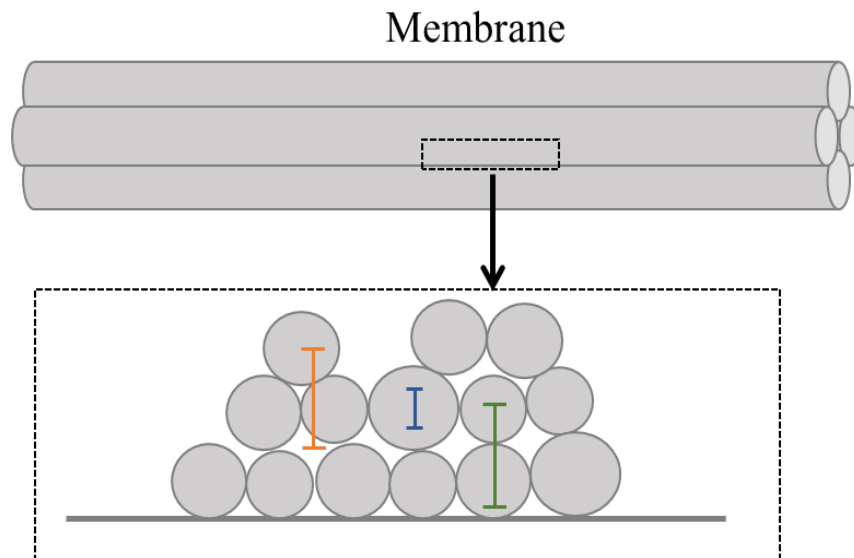


Figure 7-1. Performance of membrane separation systems depends on the transport properties of the material. A fundamental understanding on these properties at various length scales is essential when investigating novel materials for membrane based separations.

Hydrogen Sulfide (H_2S) is a toxic and corrosive gas that plagues a vast number of industrial processes ranging from natural gas processing to wastewater treatment.⁶³⁻
⁶⁴ Long term exposure to H_2S can result in adverse health effects, that vary based on its concentration.⁶⁵ It is responsible for catalyst poisoning, and corrosion of pipelines and chemical storage containers. H_2S can also form flammable mixtures that in turn produce harmful vapors such as sulfur dioxide upon ignition. It is evident that separation of H_2S is critical from both an economic and safety perspective.

Membranes have complex structures and can exhibit different transport properties at varying length scales (Figure 7-1). Advancements in membrane technology require a fundamental understanding of these distinct transport properties. This chapter presents the first microscopic diffusion study of H_2S in ZIFs as well as its influence on their transport properties due to prolonged exposure.

7.2 Diffusion of Hydrogen Sulfide

ZIF-8 is a MOF that consists of zinc ions coordinated with four imidazolate rings.⁵⁷ The large spherical cavities of ZIF-8 are accessible through small apertures that are 3.4 Å in diameter.⁶⁶ It is extensively studied due to its vast functionality and ease of assembly into various forms.^{60, 67} Given the abundant interest in ZIF-8, it was the primary focus of diffusion studies presented here.

7.2.1 Experimental Details

PFG NMR was employed to measure self-diffusivity of H_2S in ZIF-8 crystals. ZIF-8 crystals of average diameter 5.3 μm were synthesized by the group of Ryan Lively at Georgia Institute of Technology. Dr. Lively's group, fellow members of EFRC, is equipped to store and use H_2S for experimental studies. Hence, all NMR samples containing H_2S were prepared by Dr. Lively's group, at their facility.

NMR samples were prepared in a fashion similar to that described in section 4.4. Approximately 100 mg of ZIF-8 was loaded into two separate 5 mm, medium-wall, NMR tubes (Wilmad Glass) each. The tubes were then activated at an elevated temperature and evacuated under vacuum, overnight. Each tube was then attached to a manifold connected to a source of H₂S gas mixture. The gas mixture contains 5% H₂S with the remainder being N₂. The bed of ZIF-8 crystals was equilibrated with 0.9 atm of this mixture for 11 hours and subsequently immersed in liquid nitrogen to cryogenically condense H₂S into the tube. The NMR tube was then flame sealed and separated from the manifold.

¹H NMR was used to perform PFG NMR measurements of these samples. Primarily, a 600 MHz Bruker spectrometer in conjunction with a diff30 gradient probe was employed. Some experiments were also attempted on a 750 MHz Bruker spectrometer equipped with a diff50 gradient probe in an effort to reproduce results and eliminate influence of artefacts. All measurements were performed at 298 K.

7.2.2 Results and Discussion

The combination of low sorbate concentration and large susceptibility effects associated with ¹H NMR measurements in porous materials has produced many challenges in diffusion measurements of H₂S. The first obstacle was the accurate identification of H₂S signal. Acquisition of a ¹H NMR spectrum of ZIF-8 loaded with H₂S showed large baseline distortions which obscured the visibility of any distinct peak. The 13-interval PFG NMR sequence can be used to minimize the susceptibility effects and provide a more discernable spectrum. Shortening the time interval between the first and second and second and third $\pi/2$ radiofrequency pulses while applying the smallest gradient possible reveals various features. Using this procedure, the spectra shown in

Figure 7-2 were acquired and they show a distinct peak centered at 3.4 ppm. The time-evolution of this peak recorded here occurs by decreasing the time available for T_2 relaxation, i.e. the time interval between the application of the first and second $\pi/2$ radiofrequency pulses. The gradients applied were sine-shaped of amplitude 0.30 T/m.

The response of this peak to the systematic manipulation of the 13-interval sequence agrees with the predicted behavior of a real peak, uninfluenced by susceptibility effects. However, this is not enough evidence to confirm the identification of this feature as H_2S . The broad linewidth of this peak encompasses the chemical shift of bulk H_2O (4.8 ppm). While the ZIF-8 crystals were activated prior to sorbate loading, the presence of strongly adsorbed residual water is possible.

Measuring the self-diffusivity of the species that belongs to this peak can also elucidate its identity since the diffusivity of adsorbed H_2O in ZIF-8 is known (Chapter 6). Using a 600 MHz spectrometer, the 13-interval sequence (with eddy current delay) with bipolar gradients of duration 4.5 ms was employed with gradients as large as 10 T/m. A large range of diffusion times from 10 ms to 500 ms were used but with no visible attenuation of the NMR peak (Figure 7-3). This result implied a very low diffusivity of the species, several orders lower than the reported value of H_2O . Hence, the peak can be assigned to H_2S in ZIF-8.

Any further increase in experimental parameters such as gradient duration and diffusion time was limited by T_1 and T_2 relaxation processes that result in severe loss of signal. However, larger gradient strengths can be achieved using the diff50 probe that has been calibrated by our group to perform diffusion measurements in conjunction with a 750 MHz spectrometer at the AMRIS facility. This experimental setup was used to

repeat the PFG NMR measurements mentioned above. While the maximum gradient strength produced was as high as 19 T/m, the poor signal-to-noise observed at this higher spectrometer frequency restricted the magnitude of diffusion times. The largest diffusion time used at this setup was 40 ms. Under these conditions, neither the area nor intensity of the peak changed with increasing gradient strength. This confirmed the reproducibility of results at two different spectrometer frequencies, providing additional confidence in the results.

The PFG NMR measurements reported here suggest that the self-diffusivity of H₂S in ZIF-8 is extremely small. It is estimated to be less than 5×10^{-15} m²/s. Strong interactions between the ZIF-8 framework and H₂S molecules can explain this very small diffusivity. To provide further insight on a molecular scale of the strength of these interactions, this work will be continued in collaboration with Dr. J. R. Schmidt and Dr. David Sholl, fellow members of EFRC. They are currently working on MD simulations to estimate the energy associated with H₂S molecules moving from a given cage in the ZIF-8 framework to another and using this to estimate the magnitude of its self-diffusivity to compare with the experimental results discussed.

7.3 Influence of Hydrogen Sulfide Exposure on Transport Properties

Degradation of ZIF-8 crystals is a potential concern due to the corrosive nature of H₂S. Changes to the surface or bulk properties of ZIF-8 could alter the transport properties of the material. To address this issue, a comprehensive study comparing self-diffusion of various sorbates (C₂H₄ and CO₂) in pure ZIF-8 with ZIF-8 exposed to dry H₂S conditions is underway.

7.3.1 Experimental Details

Following H₂S diffusion measurements described in section 7.2, and three weeks of enclosed exposure of ZIF-8 to dry H₂S conditions, the ZIF-8 crystals were retrieved and evacuated overnight under vacuum by Dr. Lively's group. These crystals were returned to our laboratory at University of Florida for comprehensive analysis of possible influence of H₂S exposure on transport properties of ZIF-8.

To understand the effect of H₂S exposure, pure ZIF-8 crystals are compared with exposed ZIF-8, where both samples of crystals were obtained from the same synthesized batch. This was done to limit effects of heterogeneity in crystals on the observed transport properties. PFG NMR is employed to investigate self-diffusivity of C₂H₄, and CO₂ in the pre-and post-H₂S exposed samples. The NMR samples are prepared as follows. Two NMR tubes, identical to those used to prepare H₂S loaded samples as described above, were separately filled with about 95 mg of pure and 70 mg of exposed ZIF-8, respectively. The NMR tubes containing the porous material were connected to a custom-made vacuum system and any residual sorbates were removed by application of high vacuum at an elevated temperature (383 K), for 10 hours. A desired mass of each chosen sorbate was cryogenically condensed into the sample tubes using liquid nitrogen. Following sorbate loading, each tube was flame sealed and separated from the vacuum system.

Single ¹³C enriched, high purity, CO₂ and C₂H₄ gases are used as sorbates for this exposure study. The pure and exposed samples were loaded under equilibrium with a certain pressure in the gas phase. The self-diffusivity of certain sorbates has been shown to depend on its concentration. Hence, achieving equivalent adsorbed concentration, within experimental error, is essential for direct comparison of results.

The results reported here thus far pertain to C₂H₄ sorbate studies. Analysis and interpretation of CO₂ sorbate study are in progress.

The concentration of each gas in all ZIF-8 samples is determined by comparing the NMR signal of adsorbed gas in these samples with the NMR signal in an NMR tube containing only pure gas at a known pressure, in the same way as discussed in our previous work. These loadings are reported in Table 7-1 and are noted to be comparable, within experimental error.

Longitudinal (T_1) ¹³C NMR relaxation times of the adsorbed gas molecules in ZIF-8 were estimated using the 13-interval PFG NMR sequence by changing the time interval between the second and the third $\pi/2$ radiofrequency pulses of the sequence and keeping all other time intervals constant. Similarly, transverse (T_2) ¹³C NMR relaxation times were estimated using the same sequence by changing the time interval between the first and the second $\pi/2$ radiofrequency pulses of the sequence and keeping all other time intervals constant. Under the conditions of these measurements, it was confirmed that there was no attenuation of the signal due to diffusion of adsorbed gas molecules. Figure 7-4 plots the observed magnetization, normalized to the intensity of the magnetization at the smallest T_1 interval as a function of these intervals on a log-linear scale. In all of the studied samples, the measured NMR relaxation data showed a bi-exponential distribution for distribution of T_1 relaxation times for adsorbed gases. A bi-exponential curve was used to fit this data and the corresponding parameters are recorded in Table 7-2. To summarize, the larger fraction of molecules exhibit a smaller T_1 relaxation time while the smaller fraction of molecules has a larger T_1 relaxation time. The presence of two separate factions of molecules could be due to the simultaneous

presence of crystal aggregates and single-crystals. There is no apparent distribution in the T_2 relaxation values. The transverse relaxation time in pure and exposed ZIF-8 crystals was 13 ms and 14 ms, respectively. All measurements were performed at 298 K.

PFG NMR diffusion measurements were performed using a 14.0 T Bruker BioSpin NMR spectrometer operating at ^{13}C resonance frequency of 150 MHz. Selected experiments were also performed at the ^1H resonance frequency of 600 MHz. The spectrometer is located at the National High Magnetic Field Laboratory's AMRIS facility in Gainesville, FL. Sine-shaped, bipolar magnetic field gradients with the effective duration of 1.2-2.3 ms were generated using a diff30 diffusion probe (Bruker BioSpin). The range of the gradient amplitudes used was between 0.30 and 11 T/m.

7.3.2 Results and Discussion

Figure 7-5 presents examples of the measured attenuation curves for ethylene diffusion in both pure and exposed ZIF-8 obtained using ^1H and ^{13}C PFG NMR at selected diffusion times. The coincidence of the diffusion data obtained using the two nuclei rules out measurement artefacts.

At the smaller diffusion time, a bi-exponential curve corresponding to Eq 6-1 is shown to describe the data well. At the larger diffusion time, a single exponential fit provides reasonable description of the data. Table 7-3 lists the parameters of each fit at various diffusion times. The respective fractions of each diffusing ensembles are consistent with those obtained using the T_1 relaxation distribution, within the limits of experimental uncertainty. By comparison, the faster diffusing molecules exhibit a longer longitudinal relaxation time.

The diffusivity of the faster component at short diffusion times is much larger than previously reported estimates of self-diffusivity of C₂H₄ in ZIF-8.⁴¹ The slower diffusivity agrees with these published values of intra-crystalline diffusion of C₂H₄ in defect-free ZIF-8, within experimental uncertainty. Furthermore, with increasing observation time, the diffusivity of the faster molecules is shown to decrease. These observations can be rationalized by assigning the faster diffusing molecules to those diffusing a fraction of the diffusion time in macro- and mesopores (i.e. defects) between single crystals in densely packed ZIF-8 crystal aggregates. Such aggregates account for the majority of the sample as seen in the recorded SEM images in Figure 7-6. The remaining fraction of time these molecules diffuse inside ZIF-8 crystals where the diffusivity is lower. With increasing total diffusion time the fraction of time spent in macro- and mesopores by the molecules exhibiting the largest diffusivity would decrease. Hence, their diffusivity would also decrease and approach the average diffusivity inside an aggregate.

The latter, averaged, diffusivity can be similar to the intracrystalline diffusivity of ethylene in ZIF-8. Figure 7-5 presents the attenuation curves measured at longer diffusion times for both pure and exposed crystals. Due to the coincidence of all curves shown, a single mono-exponential fit was used to describe them. The corresponding self-diffusivity of ethylene molecules moving inside the crystal aggregates is $(1.1 \pm 0.8) \times 10^{-10}$ m²/s for both samples.

Based on PFG NMR measurements of ethylene in ZIF-8, there are no significant alterations in the intracrystalline structure that manifest themselves in bulk transport properties. The self-diffusivities of ethylene in ZIF-8, along with other diffusion time dependent trends, are in agreement between the pure and H₂S exposed crystals. To

reveal any alterations to surface properties, a faster diffusing sorbate such as CO₂ is appropriate.

7.4 Summary

High field and high gradient PFG NMR was applied to investigate microscopic self-diffusivity of H₂S in ZIF-8. While H₂S signal in ZIF-8 was successfully identified using ¹H NMR, its diffusivity was too low to measure with gradients as large as 19 T/m. The reported experimental data suggests the presence of strong interactions between H₂S and the ZIF-8 framework which result in a self-diffusivity that is estimated to be lower than 5 x 10⁻¹⁵ m²/s. Molecular simulation results expected to be provided by collaborators can aid in better understanding the nature of these interactions. Additionally, effects of H₂S exposure on ZIF-8 do not alter the bulk transport properties of ZIF-8 as measured using ethylene. This suggests ZIF-8 to be a stable sorbent, immune to corrosion upon exposure to small H₂S concentrations.

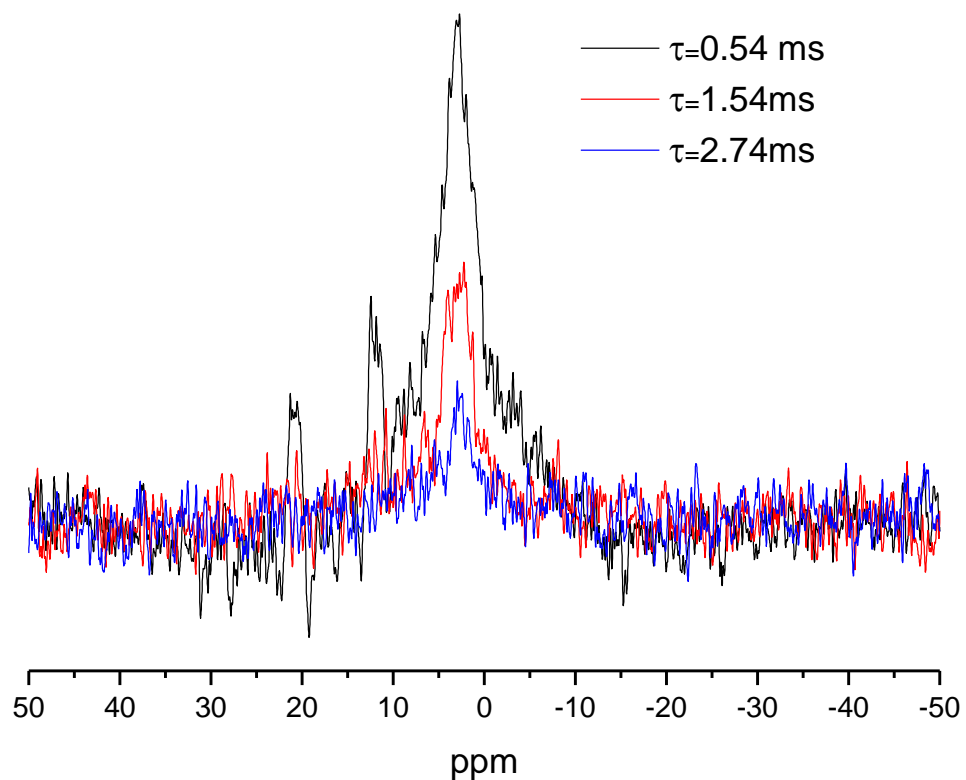


Figure 7-2. The evolution of the peak identified as H₂S in ZIF-8 acquired using the 13-interval PFG NMR sequence so that strong susceptibility effects are minimized. The time interval, τ , was systematically decreased such that various features present can be visualized.

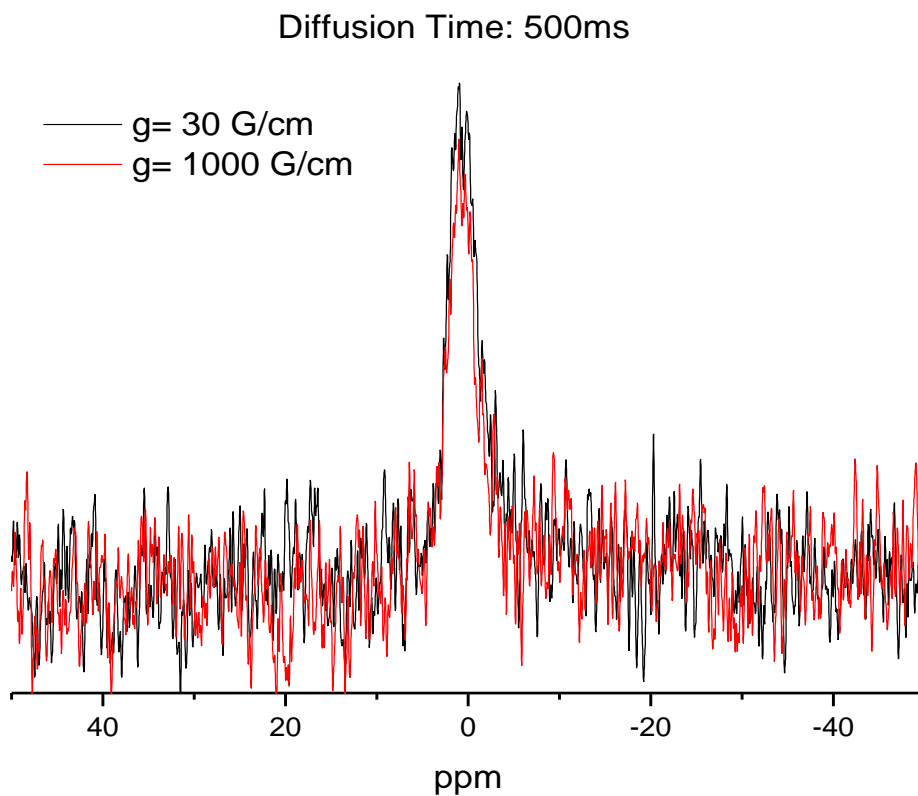
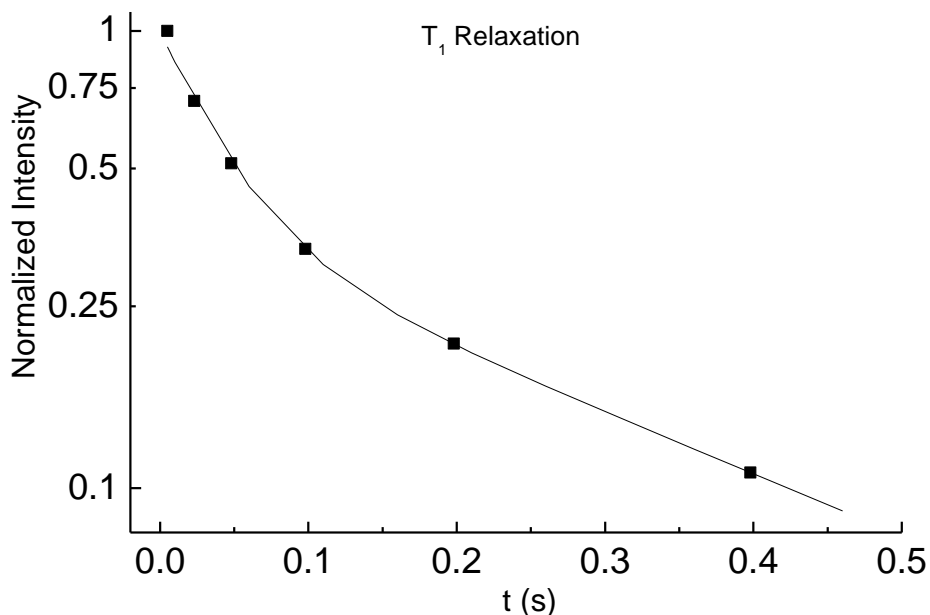


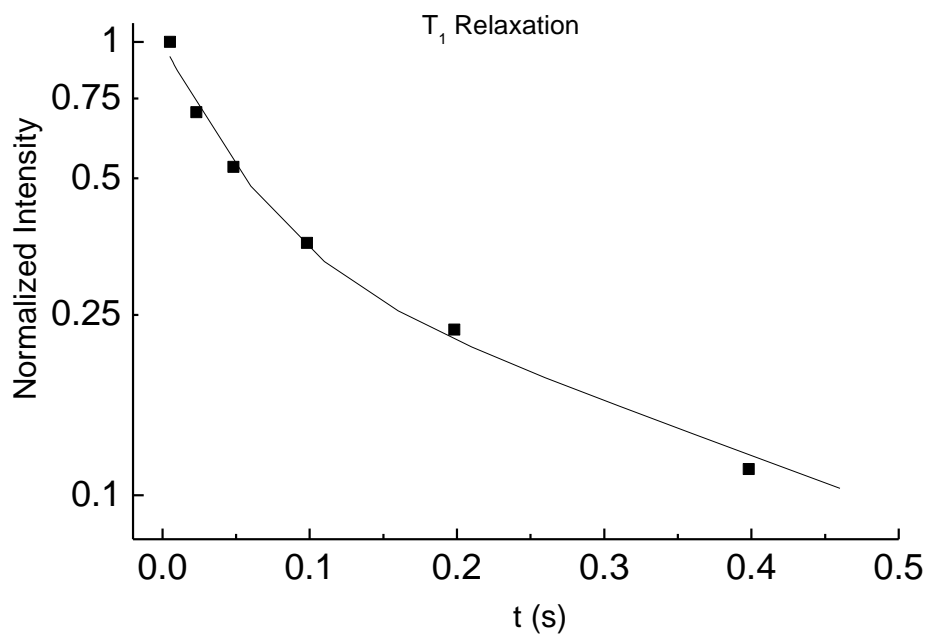
Figure 7-3. Example of ¹H spectra acquired of H₂S in ZIF-8 using the 14 T spectrometer and diff30 gradient probe. Here, the 13-interval sequence with eddy current delay was employed with the application of gradients in the range of 0.30 and 11 T/m for a diffusion time of 500 ms. No visible attenuation was observed under these and any other conditions.

Table 7-1. Concentration (mmol/g) of C₂H₄ molecules adsorbed in pure and exposed ZIF-8 crystals as determined using NMR signal analysis.

	Pure ZIF-8	Exposed ZIF-8
Ethylene (C ₂ H ₄)	2.5 ± 0.2	2.3 ± 0.2



A



B

Figure 7-4. T₁ Relaxation curves obtained using ¹³C NMR show a bi-exponential distribution in both (A) pure ZIF-8 and (B) exposed ZIF-8 crystals.

Table 7-2. The parameters corresponding to the bi-exponential curve fit to the T_1 relaxation data reported in Figure 7-4.

	Pure ZIF-8	Exposed ZIF-8
A	0.64	0.63
B	0.36	0.37
T_1 (A)	42	45
T_1 (B)	320	363

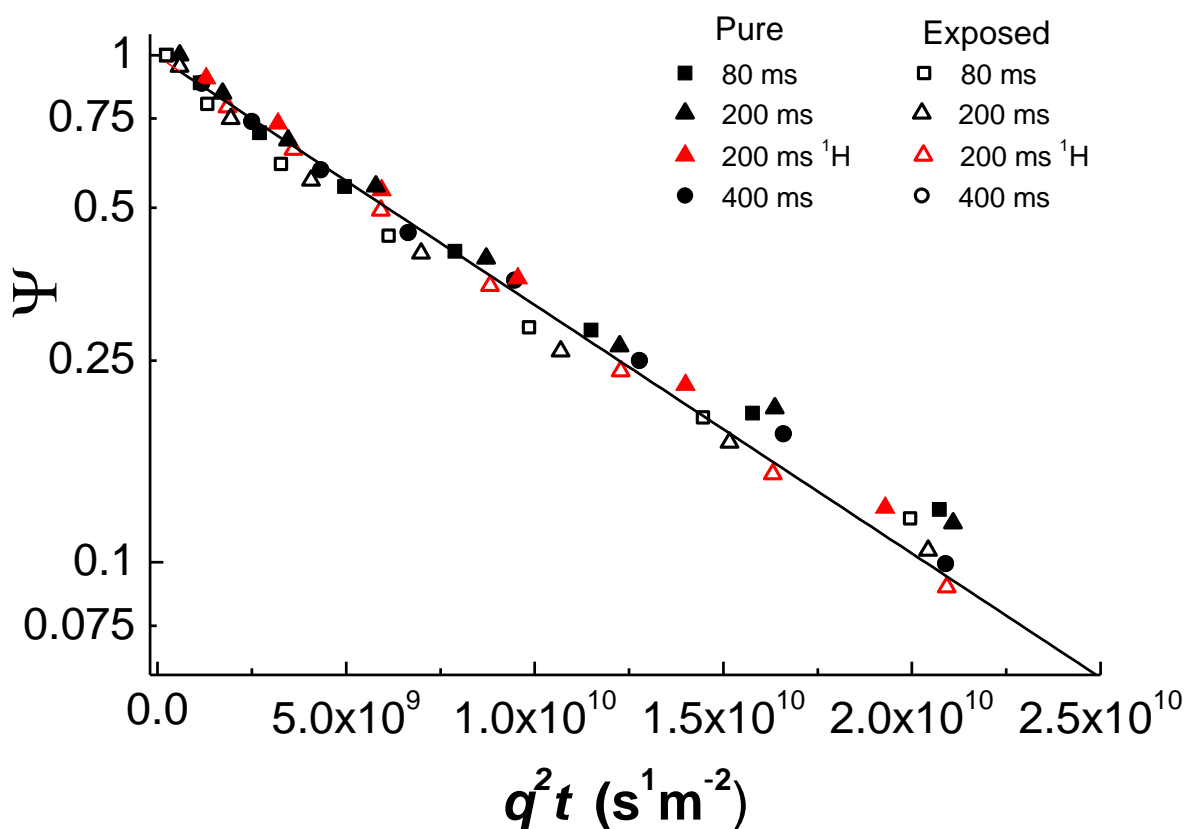


Figure 7-5. Examples of measured attenuation curves obtained using ^{13}C (black symbols) and 1H (red symbols) PFG NMR of Ethylene diffusion at 298 K in pure and exposed ZIF-8 samples. A single mono-exponential curve is fit to the data shown due to the coincidence of all attenuation curves, within experimental uncertainty.

Table 7-3. Parameters corresponding to the bi-exponential (Eq 6-1) and mono-exponential fits used to describe attenuation curves for both pure and exposed ZIF-8 at selected diffusion times.

Parameters		Diffusion Time (ms)			
		10	40	200	600
Pure ZIF-8	A	0.79 ± 0.2	0.72 ± 0.2	1	1
	B	0.21 ± 0.1	0.28 ± 0.1	0	0
	$\mathcal{D}_A \times 10^{-11}$ (m ² /s)	8.9 ± 1.5	8.3 ± 1.2	11 ± 2	10 ± 2
	$\mathcal{D}_B \times 10^{-11}$ (m ² /s)	53 ± 8	24 ± 3	0	0
Exposed ZIF-8	A	0.68 ± 0.1	0.65 ± 0.1	0.72 ± 0.2	1
	B	0.32 ± 0.1	0.35 ± 0.1	0.28 ± 0.1	0
	$\mathcal{D}_A \times 10^{-11}$ (m ² /s)	8.7 ± 1.5	8.4 ± 1.5	9.4 ± 2.0	12 ± 2
	$\mathcal{D}_B \times 10^{-11}$ (m ² /s)	51 ± 7	37 ± 4	24 ± 4	0

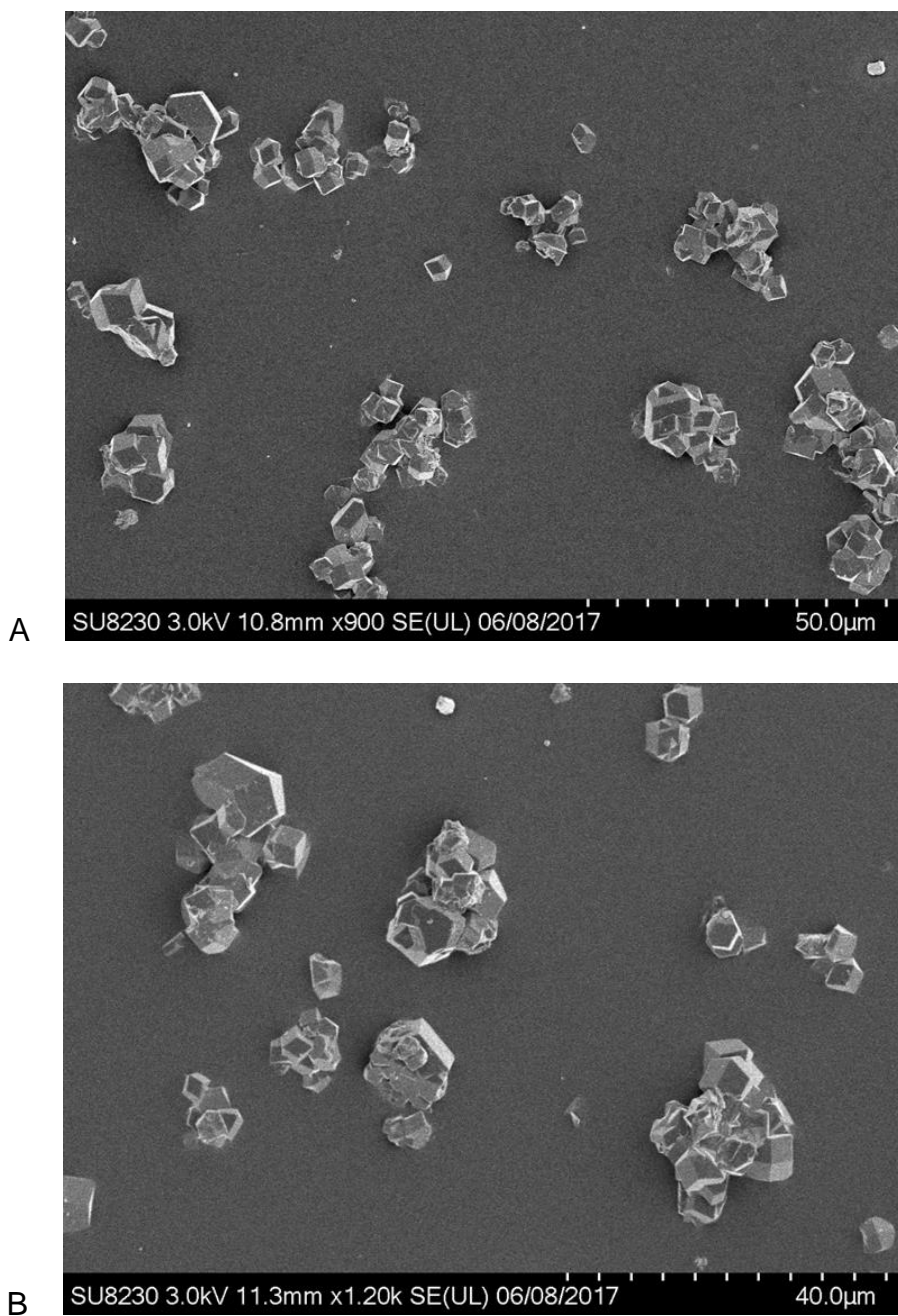


Figure 7-6. SEM images provided by collaborators in Dr. Ryan Lively's group of (A) pure and (B) exposed ZIF-8. These images show that both samples consist largely of aggregates of crystals. No significant differences are observed between the pure and exposed samples.

CHAPTER 8 CONCLUSIONS

Gas separation processes can be an energetically expensive process when conducted using thermally driven technologies. The main focus of this dissertation was to investigate the fundamentals of a conceptually novel process of gas separations that offers an energetically favorable alternative. It is based on the induction of single-file diffusion of a chosen sorbate in a mixture which can result in highly-selective separations. Single-file diffusion of sorbate mixtures was observed and reported for the first time using diffusion NMR that combined high magnetic field and large field gradients. The following gases were studied in an ideal system of microporous channels as single-sorbate and mixtures: CO, CO₂, and CH₄.

SFD of all components of single-sorbate and mixture samples of CO/CO₂ and CO/CH₄ was confirmed by the growth of their mean-squared displacement with the square root of diffusion time, a unique signature of single-file motion. Additionally, the rates of SFD of both components in a given mixture are identical, within experimental uncertainty, as expected under single-file confinement where molecules cannot pass each other. As single-sorbate samples, each gas exhibited a distinct rate of single-file diffusion. The collective single-file mobility of the mixture components is shown to be intermediate of its respective components in pure form. This trend is qualitatively different from the case of normal diffusion in microporous materials where an addition of a faster-diffusing component to a slower-diffusing component does not change significantly the diffusivity of the slower-diffusing component.

The predictions of a random walk model describe a transition from SFD to center-of-mass diffusion in finite channels under the SFD conditions. However, this

transition is not experimentally observed for the systems studied. Molecular clustering is proposed to explain the absence of such a transition. The minimum cluster size needed to maintain the SFD regime observed under the experimental conditions reported here was estimated to be in the range of 30 and 140 molecules. The presence of molecular clusters is also shown to offer a plausible explanation for the relationship experimentally observed between the one-component and mixture mobilities.

Hydrogen sulfide, a hazardous impurity, often needs to be isolated and removed for both economic and safety reasons. ZIFs are promising candidates for such a separation and the microscopic diffusion of H₂S in ZIF-8 was investigated here. Preliminary measurements reveal the self-diffusivity of H₂S to be lower than 5×10^{-15} m²/s. This extremely low diffusivity could be a result of strong interactions between the sorbate and the ZIF-8 framework. The potential influence of exposure to H₂S on the transport properties of ZIF-8 was also studied. Comparison of the trends of self-diffusion of ethylene in pure and exposed ZIF-8 did not reveal any alteration of the bulk transport properties of the microporous sorbent. Further analysis of changes in the external surface properties is currently underway by comparison of self-diffusivity of carbon dioxide in pure and exposed ZIF-8 crystals.

In an effort to overcome some of the limitations of standard diffusion NMR associated with studying sorbates in porous materials, an experimental setup that combines magic-angle spinning with PFG NMR was introduced at the National High Magnetic Field Laboratory. A high-resolution MAS probe equipped with gradients was calibrated and tested to perform diffusion measurements. The maximum gradient strength of the probe was determined to be 0.56 ± 0.01 T/m and the gradient field was

shown to be uniform along the bulk of the rotor length. Changes in the temperature of the sample due to the mechanical heating that results from high spinning rates was also evaluated. Finally, the accuracy of the reported calibration procedure was assessed by demonstrating the agreement between self-diffusivity of H₂O in ZIF-8 between PFG NMR under static and magic angle spinning conditions.

LIST OF REFERENCES

1. *Materials for Separation Technologies. Energy and Emission Reduction Opportunities*; Oak Ridge National Lab. (ORNL), Oak Ridge, TN (United States): 2005.
2. Humphrey, J.; Keller, G. E., *Separation Process Technology*; McGraw-Hill, 1997.
3. Bernardo, P.; Drioli, E.; Golemme, G., Membrane Gas Separation: A Review/State of the Art. *Ind. Eng. Chem. Res.* **2009**, *48*, 4638-4663.
4. Nagai, K.; Lee, Y. M.; Masuda, T., *Polymeric Membranes for Gas Separation, Water Purification and Fuel Cell Technology*; J. Wiley-VCH, 2007.
5. Pérez-Ramírez, J.; Christensen, C. H.; Egeblad, K.; H., C. C.; C., G. J., Hierarchical Zeolites: Enhanced Utilisation of Microporous Crystals in Catalysis by Advances in Materials Design. *Chem. Soc. Rev.* **2008**, DOI: 10.1039/b809030k.
6. Auerbach, S. M.; Carrado, K. A.; Dutta, P. K., *Handbook of Zeolite Science and Technology*. Marcel Dekker, Inc.: New York, Basel, 2003; p 341-423.
7. Incropera, F. P., *Fundamentals of Heat and Mass Transfer*, 6th ed.; J. Wiley: Hoboken, 2007.
8. Bird, R. B.; Stewart, W. E.; Lightfoot, E. N., *Transport Phenomena*, 2nd ed.; J. Wiley: New York, 2002.
9. Chandler, D., *Introduction to Modern Statistical Mechanics*; Oxford University Press: New York, 1987.
10. Einstein, A., Über Die Von Der Molekularkinetischen Theorie Der Wärme Geforderte Bewegung Von in Ruhenden Flüssigkeiten Suspendierten Teilchen. *Ann. Phys.* **1905**, *322*, 549-560.
11. Krishna, R., Describing the Diffusion of Guest Molecules inside Porous Structures. *J. Phys. Chem. C.* **2009**, *113*, 19756-19781.
12. Kärger, J.; Ruthven, D. M.; Theodorou, D. N., *Diffusion in Nanoporous Materials*; Wiley-VCH Verlag GmbH & Co. KGaA: Weinheim, Germany, 2012.
13. Nelson, P. H.; Auerbach, S. M., Self-Diffusion in Single-File Zeolite Membranes Is Fickian at Long Times. *J. Chem. Phys.* **1999**, *110*, 9235-9243.
14. Delfau, J.-B.; Coste, C.; Saint Jean, M., Single-File Diffusion of Particles with Long-Range Interactions: Damping and Finite-Size Effects. *Phys. Rev. E.* **2011**, *84*, 011101.
15. Hahn, K.; Kärger, J., Deviations from the Normal Time Regime of Single-File Diffusion. *J. Phys. Chem.* **1998**, *102*, 5766-5771.

16. Atkins, P. W.; De Paula, J., *Atkins' Physical Chemistry*, 8th ed.; Oxford University Press: Oxford, 2006.
17. Levitt, M. H., *Spin Dynamics: The Basics of Nuclear Magnetic Resonance*, 2nd ed.; J. Wiley, 2007.
18. Halliday, D.; Resnick, R.; Walker, J., *Fundamentals of Physics*, 7th ed.; J. Wiley: Hoboken, 2005.
19. Stejskal, E. O.; Tanner, J. E., Spin Diffusion Measurements: Spin Echoes in the Presence of a Time-Dependent Field Gradient. *J. Chem. Phys.* **1965**, *42*, 288-292.
20. Tanner, J. E., Use of the Stimulated Echo in Nmr Diffusion Studies. *J. Chem. Phys.* **1970**, *52*, 2523-2526.
21. Cotts, R. M.; Hoch, M. J. R.; Sun, T.; Markert, J. T., Pulsed Field Gradient Stimulated Echo Methods for Improved Nmr Diffusion Measurements in Heterogeneous Systems. *J. Magn. Reson.* **1989**, *83*, 252-266.
22. Wei, Q. H.; Bechinger, C.; Leiderer, P., Single-File Diffusion of Colloids in One-Dimensional Channels. *Science*. **2000**, *287*, 625.
23. Yang, S. Y.; Yang, J.-A.; Kim, E.-S.; Jeon, G.; Oh, E. J.; Choi, K. Y.; Hahn, S. K.; Kim, J. K., Single-File Diffusion of Protein Drugs through Cylindrical Nanochannels. *ACS. Nano*. **2010**, *4*, 3817-3822.
24. Lei, G. D.; Carvill, B. T.; Sachtler, W. M. H., Single File Diffusion in Mordenite Channels: Neopentane Conversion and H/D Exchange as Catalytic Probes. *Appl. Catal., A*. **1996**, *142*, 347-359.
25. Kärger, J.; Petzold, M.; Pfeifer, H.; Ernst, S.; Weitkamp, J., Single-File Diffusion and Reaction in Zeolites. *J. Catal.* **1992**, *136*, 283-299.
26. Sholl, D. S.; Fichthorn, K. A., Normal, Single-File, and Dual-Mode Diffusion of Binary Adsorbate Mixtures in Alpo4-5. *J. Chem. Phys.* **1997**, *107*, 4384-4389.
27. Adhangale, P.; Keffer, D., Exploiting Single-File Motion in One-Dimensional Nanoporous Materials for Hydrocarbon Separation. *Sep. Sci. Technol.* **2003**, *38*, 977-998.
28. Keffer, D., The Temperature Dependence of Single - File Separation Mechanisms in One-Dimensional Nanoporous Materials. *Chem. Eng. J.* **1999**, *74*, 33-42.
29. Wanasundara, S. N.; Spiteri, R. J.; Bowles, R. K., Single File and Normal Dual Mode Diffusion in Highly Confined Hard Sphere Mixtures under Flow. *J. Chem. Phys.* **2012**, *137*, 104501.

30. Okino, M. S.; Snurr, R. Q.; Kung, H. H.; Ochs, J. E.; Mavrovouniotis, M. L., A Consistent Correlation Approach to Single File Diffusion with Reaction. *J. Chem. Phys.* **1999**, *111*, 2210-2221.
31. Liu, D.-J.; Wang, J.; Ackerman, D. M.; Slowing, I. I.; Pruski, M.; Chen, H.-T.; Lin, V. S. Y.; Evans, J. W., Interplay between Anomalous Transport and Catalytic Reaction Kinetics in Single-File Nanoporous Systems. *ACS. Catal.* **2011**, *1*, 751-763.
32. Broadbelt, L. J.; Snurr, R. Q., Applications of Molecular Modeling in Heterogeneous Catalysis Research. *Appl. Catal., A.* **2000**, *200*, 23-46.
33. Neugebauer, N.; Bräuer, P.; Kärger, J., Reactivity Enhancement by Molecular Traffic Control. *J. Catal.* **2000**, *194*, 1-3.
34. Rödenbeck, C.; Kärger, J.; Hahn, K., Tracer Exchange and Catalytic Reaction in Single-File Systems. *J. Catal.* **1995**, *157*, 656-664.
35. Nelson, P. H.; Auerbach, S. M., Modeling Tracer Counter-Permeation through Anisotropic Zeolite Membranes: From Mean-Field Theory to Single-File Diffusion. *Chem. Eng. J.* **1999**, *74*, 43-56.
36. Rao, S. M.; Coppens, M.-O., Predicting Mixture Diffusion in Zeolites: Capturing Strong Correlations with a Simplified Theory and Examining the Role of Adsorption Thermodynamics. *J. Phys. Chem. C.* **2012**, *116*, 26816-26821.
37. Chen, Q.; Moore, J. D.; Liu, Y.-C.; Roussel, T. J.; Wang, Q.; Wu, T.; Gubbins, K. E., Transition from Single-File to Fickian Diffusion for Binary Mixtures in Single-Walled Carbon Nanotubes. *J. Chem. Phys.* **2010**, *133*, 094501.
38. Soldatov, D. V.; Moudrakovski, I. L.; Ripmeester, J. A., Dipeptides as Microporous Materials. *Angew. Chem., Int. Ed.* **2004**, *43*, 6308-6311.
39. Dvoyashkin, M.; Wang, A.; Katihar, A.; Zang, J.; Yucelen, G. I.; Nair, S.; Sholl, D. S.; Bowers, C. R.; Vasenkov, S., Signatures of Normal and Anomalous Diffusion in Nanotube Systems by Nmr. *Microporous Mesoporous Mater.* **2013**, *178*, 119-122.
40. Mehio, N.; Dai, S.; Jiang, D.-e., Quantum Mechanical Basis for Kinetic Diameters of Small Gaseous Molecules. *J. Phys. Chem. A.* **2014**, *118*, 1150-1154.
41. Mueller, R.; Hariharan, V.; Zhang, C.; Lively, R.; Vasenkov, S., Relationship between Mixed and Pure Gas Self-Diffusion for Ethane and Ethene in Zif-8/6fda-Dam Mixed-Matrix Membrane by Pulsed Field Gradient Nmr. *J. Membr. Sci.* **2016**, *499*, 12-19.
42. Dvoyashkin, M.; Wang, A.; Vasenkov, S.; Bowers, C. R., Xenon in L-Alanyl-L-Valine Nanochannels: A Highly Ideal Molecular Single-File System. *J. Phys. Chem. Lett.* **2013**, *4*, 3263-3267.

43. Moudrakovski, I.; Soldatov, D. V.; Ripmeester, J. A.; Sears, D. N.; Jameson, C. J., Xe Nmr Lineshapes in Channels of Peptide Molecular Crystals. *Proc. Natl. Acad. Sci.* **2004**, *101*, 17924-17929.
44. Sholl, D. S.; Lee, C. K., Influences of Concerted Cluster Diffusion on Single-File Diffusion of Cf₄ in Alpo₄₋₅ and Xe in Alpo₄₋₃₁. *J. Chem. Phys.* **2000**, *112*, 817-824.
45. Sholl, D. S.; Fichthorn, K. A., Concerted Diffusion of Molecular Clusters in a Molecular Sieve. *Phys. Rev. Lett.* **1997**, *79*, 3569-3572.
46. Sholl, D. S., Characterization of Molecular Cluster Diffusion in Alpo₄₋₅ Using Molecular Dynamics. *Chem. Phys. Lett.* **1999**, *305*, 269-275.
47. Chmelik, C.; Bux, H.; Caro, J.; Heinke, L.; Hibbe, F.; Titze, T.; Kärger, J., Mass Transfer in a Nanoscale Material Enhanced by an Opposing Flux. *Phys. Rev. Lett.* **2010**, *104*, 085902.
48. Fernandez, M.; Kärger, J.; Freude, D.; Pampel, A.; van Baten, J. M.; Krishna, R., Mixture Diffusion in Zeolites Studied by Mas Pfg Nmr and Molecular Simulation. *Microporous Mesoporous Mater.* **2007**, *105*, 124-131.
49. Pampel, A.; Fernandez, M.; Freude, D.; Kaerger, J., New Options for Measuring Molecular Diffusion in Zeolites by Mas Pfg Nmr. *Chem. Phys. Lett.* **2005**, *407*, 53-57.
50. Fernandez, M.; Kärger, J.; Freude, F.; Pampel, A.; van Baten, J. M.; Krishna, R., Mixture Diffusion in Zeolites Studied by Mas Pfg Nmr and Molecular Simulation. *Microporous Mesoporous Mater.* **2007**, *105*, 124-131.
51. Fernandez, M.; Pampel, A.; Takahashi, R.; Sato, S.; Freude, D.; Kärger, J., Revealing Complex Formation in Acetone–N-Alkane Mixtures by Mas Pfg Nmr Diffusion Measurement in Nanoporous Hosts. *PCCP.* **2008**, *10*, 4165-4171.
52. Chmelik, C.; Freude, D.; Bux, H.; Haase, J., Ethene/Ethane Mixture Diffusion in the Mof Sieve Zif-8 Studied by Mas Pfg Nmr Diffusometry. *Microporous Mesoporous Mater.* **2012**, *147*, 135-141.
53. Arzumanov, S. S.; Kolokolov, D. I.; Freude, D.; Stepanov, A. G., Methane Mobility in Ag/H-Zsm-5 Zeolite in the Presence of Ethene: A View Based on Pfg 1h Mas Nmr Analysis of Methane Diffusivity. *J. Phys. Chem. C.* **2015**, *119*, 18481-18486.
54. Viel, S.; Ziarelli, F.; Pagès, G.; Carrara, C.; Caldarelli, S., Pulsed Field Gradient Magic Angle Spinning Nmr Self-Diffusion Measurements in Liquids. *J. Magn. Reson.* **2008**, *190*, 113-123.
55. Hurd, R. E.; Deese, A.; Johnson, M. O. N.; Sukumar, S.; van Zijl, P. C. M., Impact of Differential Linearity in Gradient-Enhanced Nmr. *J. Magn. Reson.* **1996**, *119*, 285-288.

56. Ammann, C.; Meier, P.; Merbach, A., A Simple Multinuclear Nmr Thermometer. *J. Magn. Reson.* **1982**, *46*, 319-321.
57. Chen, B.; Yang, Z.; Zhu, Y.; Xia, Y., Zeolitic Imidazolate Framework Materials: Recent Progress in Synthesis and Applications. *J. Mat. Chem. A.* **2014**, *2*, 16811-16831.
58. Thompson, J. A.; Blad, C. R.; Brunelli, N. A.; Lydon, M. E.; Lively, R. P.; Jones, C. W.; Nair, S., Hybrid Zeolitic Imidazolate Frameworks: Controlling Framework Porosity and Functionality by Mixed-Linker Synthesis. *Chem. Mater.* **2012**, *24*, 1930-1936.
59. Banerjee, R.; Phan, A.; Wang, B.; Knobler, C.; Furukawa, H.; O'Keeffe, M.; Yaghi, O. M., High-Throughput Synthesis of Zeolitic Imidazolate Frameworks and Application to Co₂ Capture. *Science.* **2008**, *319*, 939-943.
60. Park, K. S.; Ni, Z.; Côté, A. P.; Choi, J. Y.; Huang, R.; Uribe-Romo, F. J.; Chae, H. K.; O'Keeffe, M.; Yaghi, O. M., Exceptional Chemical and Thermal Stability of Zeolitic Imidazolate Frameworks. *Proc. Natl. Acad. Sci.* **2006**, *103*, 10186-10191.
61. Bux, H.; Liang, F.; Li, Y.; Cravillon, J.; Wiebcke, M.; Caro, J. r., Zeolitic Imidazolate Framework Membrane with Molecular Sieving Properties by Microwave-Assisted Solvothermal Synthesis. *J. Am. Chem. Soc.* **2009**, *131*, 16000-16001.
62. Bux, H.; Feldhoff, A.; Cravillon, J.; Wiebcke, M.; Li, Y.-S.; Caro, J., Oriented Zeolitic Imidazolate Framework-8 Membrane with Sharp H₂/C₃H₈ Molecular Sieve Separation. *Chem. Mater.* **2011**, *23*, 2262-2269.
63. Waernbaum, G.; Wallin, I., Hazards in the Work Environment—Hydrogen Sulfide: Spectrophotometric Determination of Hydrogen Sulfide. *Scand. J. Work Environ. Health.* **1979**, 31-34.
64. Guidotti, T., Hydrogen Sulphide. *Occup. Med.* **1996**, *46*, 367-371.
65. Guidotti, T. L., Hydrogen Sulfide: Advances in Understanding Human Toxicity. *Intl. J. Toxicol.* **2010**, *29*, 569-581.
66. Banerjee, R.; Furukawa, H.; Britt, D.; Knobler, C.; O'Keeffe, M.; Yaghi, O. M., Control of Pore Size and Functionality in Isorecticular Zeolitic Imidazolate Frameworks and Their Carbon Dioxide Selective Capture Properties. *J. Am. Chem. Soc.* **2009**, *131*, 3875-3877.
67. Lu, G.; Hupp, J. T., Metal– Organic Frameworks as Sensors: A Zif-8 Based Fabry–Pérot Device as a Selective Sensor for Chemical Vapors and Gases. *J. Am. Chem. Soc.* **2010**, *132*, 7832-7833.

BIOGRAPHICAL SKETCH

Akshita Ranjan Dutta was born in Aligarh, India to Ranjan and Mini Dutta. She spent the first eight years of her life in India before relocating to Hong Kong with her family. She was raised there along with her younger brother, Mudit Dutta. As she was about to enter high school, she once again relocated, this time to Florida. After completing her high school education at Coral Glades High school in Coral Springs in 2009, she was accepted to pursue a B.S. in chemical engineering at the University of California, Berkeley.

While at Berkeley, Akshita had the opportunity to engage in various undergraduate research opportunities in various fields related to alternative energy. Some of her research accomplishments include participation in the REU program at the National High Magnetic Field Laboratory and an international research internship at the Indian Institute of Technology in Kharagpur, India. She was an active member of the Berkeley chapter of American Institute of Chemical Engineering and served as an officer for two years. She graduated from UC Berkeley with a B.S. in chemical engineering in May 2013.

Following the completion of her undergraduate degree, she joined the University of Florida's Department of Chemical Engineering to pursue a doctoral degree. In September of 2013, Akshita joined the labs of Dr. Sergey Vasenkov and Dr. Kirk J. Ziegler to study transport of molecules subjected to extreme conditions in porous materials. She has shared her research with colleagues through numerous poster and oral presentations at various conferences. She was awarded 3rd place in AIChE TED Separations competition in 2016.

During the completion of her doctoral studies, Akshita mentored several undergraduate and masters' students interested in academic research. She also served as a teaching assistant and was awarded Outstanding Teaching Assistant of the Year for the 2016 Spring Semester. Akshita has been involved in several outreach programs that promote interest in science of elementary, middle, and high school students.